# TRANSATOMIC

## TPX MICROREACTOR

## DESIGN OVERVIEW WHITE PAPER

JULY 2018

V 0.1

*TPX builds on the inherent safety advantages of liquid fuel with a cost-effective, simplified microreactor design. TPX is an integral reactor that uses natural circulation and has a variable power output of 5 - 25 MWth. The reactor is passively safe and has a high capacity factor due to its long refueling intervals and minimal maintenance requirements. It uses commercially available enrichment processes and produces minimal tritium. Based on its the small size, simplified design and low cost, TPX looks to capture the alternative energy market for unique applications such as data centers, mining, microgrids, and critical infrastructure.*

# Contents

# 1. Introduction

Today's nuclear industry is burdened by cost overruns and project delays, due in part to the intricate and complex safety requirements that stem from the use of solid fuel in advanced light water reactors. In the 1950s and 1960s two liquid fueled molten salt reactors, the Aircraft Reactor Experiment (ARE) and the Molten Salt Reactor Experiment (MSRE) were constructed and operated. [1] These systems showed, among other things, that the emergency cooling requirements for a liquid fuel could be greatly simplified as a result of the convective nature of the fluid. Although promising in terms of the safety potential, molten salt reactors can require costly, complex systems and components in other areas of the design, most notably in regard to chemical processing, material compatibility, and special nuclear material accounting.

TPX looks to build on the inherent safety advantages of liquid fuel while employing a cost-effective, simplified design that is built to succeed in today's energy market. TPX is an integral, very Small Modular Reactor (vSMR), [2] that runs entirely on natural circulation and has a variable power output (5 - 25 $MW_{th}$). The reactor is passively safe, and has both a high capacity factor as a result of its long refueling intervals (2500 $TW_{th}h$) and minimal maintenance requirements. It uses commercially available enrichment processes (e.g. $^{7}Li$, $^{37}Cl$, $^{235}U$ > 5%), and produces minimal tritium. Based on its the small size, simplified design and low cost, TPX looks to capture the alternative energy market for unique applications such as data centers, mining, microgrids, and critical infrastructure.

A summary of the key design parameters for the TPX reactor is shown in Table 1.1, with the sections that follow outlining the design process and selection criteria.

Table 1.1 Key design parameters of the TPX reactor

| | |
|---|---|
| **General** | |
| Reactor Type | Molten Salt Reactor |
| Neutron Spectrum | Thermal |
| Power ($MW_{th}$) | 5 – 25 |
| **Materials** | |
| Fuel Salt | $NaF\text{-}ZrF_4\text{-}UF_4$ |
| Coolant Salt | $NaF\text{-}ZrF_4$ |
| Moderator | Zirconium Hydride ($ZrH_{1.66}$) |
| **Thermal Hydraulics** | |
| Heat Exchanger Type | Helical Coil |
| Driving Force | Natural Circulation |
| Operational Temperature Range (°C) | 600 – 700 |
| **Vessel Geometry** | |
| Vessel Type | Integral |
| Height (m) | 3.25 |
| Diameter (m) | 2.10 |

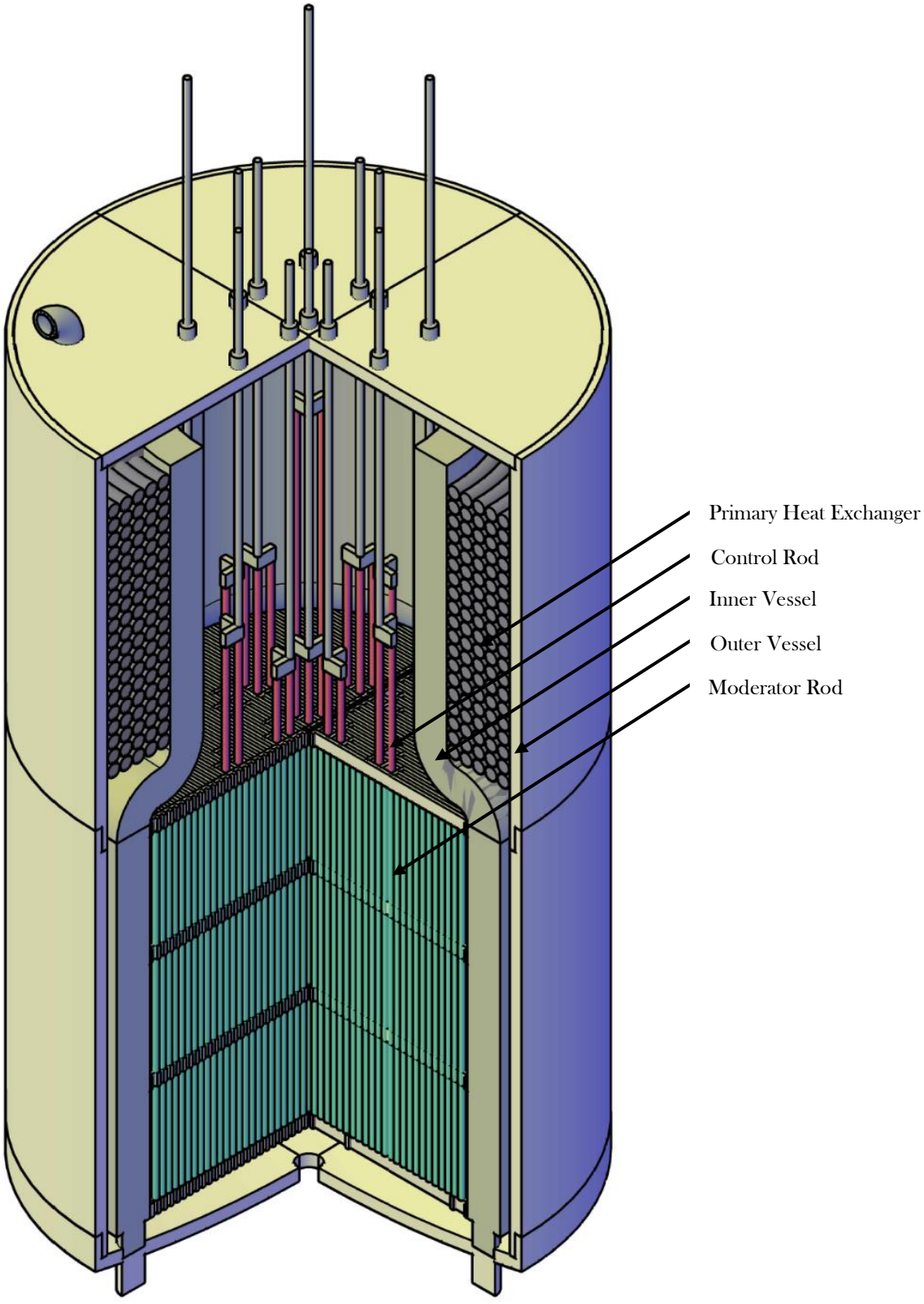


Figure 1.1 Conceptual 3D rendering of the TPX integral reactor vessel.

# 2. Salt Selection

Salt selection was made by considering neutronics, thermal hydraulics, material compatibility, vapor pressure and cost. A summary of the fuel and coolant salt compositions and thermal physical properties is shown in Tables 2.1 and 2.2.

Table 2.1 A summary of the fuel salt's composition and properties. For more information on property determination see Appendix A.

| Composition (Mole Fraction, $X_i$) | |
|---|---|
| NaF | 0.504 |
| $ZrF_4$ | 0.364 |
| $UF_4$ | 0.132 |
| **Thermal-Physical Properties** | |
| Melting Temperature (°C) | 550 |
| Density* (kg $m^{-3}$) | 3772 |
| Thermal Expansion Coefficient* ($°C^{-1}$) | 0.000277 |
| Heat Capacity (J $kg^{-1}$ $°C^{-1}$) | 946 |
| Thermal Conductivity (W $m^{-1}$ $°C^{-1}$) | 0.81 |
| Viscosity* (Pa s) | 0.0098 |

* Values have been given for the expected minimum operational temperature of 600 °C

Table 2.2 A summary of the coolant salt's compositions and properties. For more information on property determination see Appendix A.

| Composition (Mole Fraction, $X_i$) | |
|---|---|
| NaF | 0.595 |
| $ZrF_4$ | 0.405 |
| **Thermal Physical Properties** | |
| Melting Temperature (°C) | 500 |
| Density** (kg $m^{-3}$) | 3099 |
| Thermal Expansion Coefficient** ($°C^{-1}$) | 0.000314 |
| Heat Capacity (J $kg^{-1}$ $°C^{-1}$) | 1161 |
| Thermal Conductivity (W $m^{-1}$ $°C^{-1}$) | 0.84 |
| Viscosity** (Pa s) | 0.0091 |

** Values have been given for the expected minimum operational temperature of 550 °C

## 2.1 Absorption Cross Section

In 1970, the director of the reactor chemistry division at the Oak Ridge National Laboratory (ORNL), Warren Grimes, proposed some selection criteria for the use of molten salts in reactor applications. [3] At the time, an emphasis was placed on the breeding performance of the fuel salt, causing many viable options to be passed over. Specifically, isotopes that had higher absorption cross-sections then $^{7}$Li were deemed unfit to serve as a major constituent of the fuel salt. If this criterion is removed, a wider range of material combinations are available to meet the demands of the current industry (Table 2.2).

Table 2.2 Elements or isotopes which may be tolerable in high-temperature reactor fuels. [3]

| Material | Thermal Neutron Absorption Cross Section (barns) |
|---|---|
| $^{15}N$ | 0.000024 |
| O | 0.0002 |
| $^{2}H$ | 0.00057 |
| C | 0.0033 |
| F | 0.009 |
| Be | 0.01 |
| Bi | 0.032 |
| $^{7}Li$ | 0.033 |
| $^{11}B$ | 0.05 |
| Mg | 0.063 |
| Si | 0.13 |
| Pb | 0.17 |
| Zr | 0.18 |
| P | 0.21 |
| Al | 0.23 |
| $^{1}H$ | 0.33 |
| Ca | 0.43 |
| S | 0.49 |
| Na | 0.53 |
| $^{37}Cl$ | 0.56 |
| Sn | 0.6 |
| Ce | 0.7 |
| Rb | 0.7 |

## 2.2 Melting Point

To balance the introduction of more parasitic constituents, higher fractions of fissile material are required to achieve and maintain criticality. As higher concentrations of uranium tend to lead to higher melting points, certain salt combinations are eliminated based on the practicality of their operational temperature range. For TPX, it was decided that in order to limit the temperature of the moderator and structural materials, only salts that melt at or below 550 °C would be considered. If it is later determined that this value is overly conservative, additional higher-melting-point compositions can be explored.

Coolant salts can be thought of as facilitating safe interaction between the fuel and power cycle, both in term of a barrier to radioactive release and as a thermal buffer. As a result, having a salt that can operate in a wide range of operational temperatures is ideal.

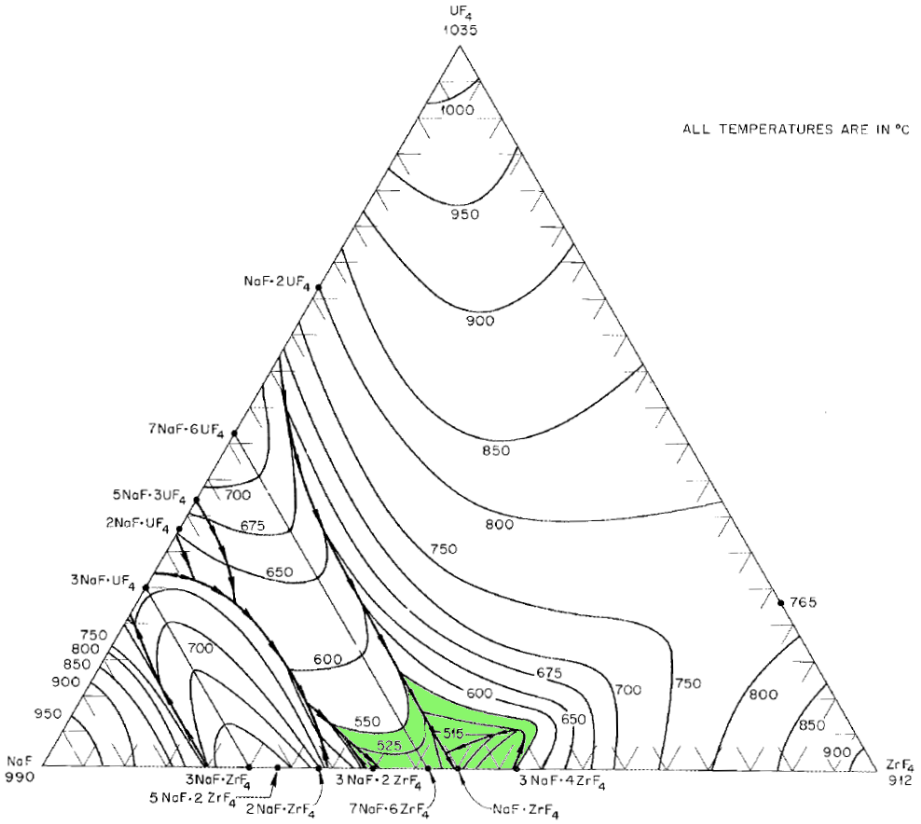


Figure 2.1 The NaF-$ZrF_4$-$UF_4$ phase diagram, with the compositional range that melts below 550°C shown highlighted in green. [4]

## 2.3 Acid-Base Chemistry

As TPX looks to reduce the complexity of the reactor as a whole, priority has been given to fuel and coolant salts that both have a low vapor pressure and exhibit good inherent corrosion performance. If the acidity of the solution is appropriately selected, it is possible that external redox control may not be required for the regulation of corrosion and $UF_3$ solubility.

When moving away from the realm of aqueous solutions, the role of acid-base chemistry is something that can often be forgotten in the early stages of the design process. However, despite the limited experience with molten salts, the acid-base nature of these systems has already been used to explain the trends observed in several key design parameters such as corrosion performance and vapor pressure. [5] [6] [7]

In molten salts, basic species (electron pair donors) such as the alkali halides, (e.g. NaF) can complex with the more acidic constituents (electron pair acceptors, e.g. $ZrF_4$) present in solution. This complexation has been used to describe the non-linear trend in vapor pressure (Figure 2.2) that has been observed as a function of composition, by indicating that the volatile acidic constituents are stabilized. [8]

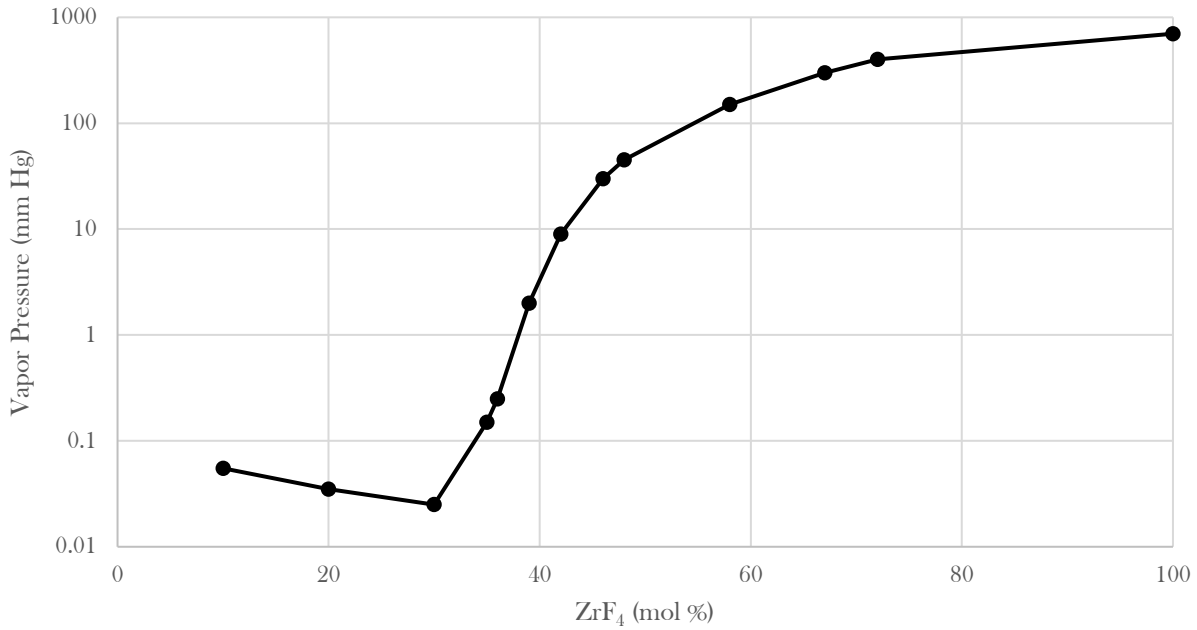


Figure 2.2 Vapor pressure at 900 °C as a function of the mol % of $ZrF_4$ in the NaF-$ZrF_4$ system. Please note the figure has been adapted from [5]. $UF_4$ is expected to act as a weak acid due to its low charge density, and unfavorable $UF_5$ coordination structure.

The acid-base ratio of these components can also be shown to affect several secondary equilibria within these systems, specifically, the stability of corrosion products such as $CrF_2$ (Table 2.3). Extremely basic solutions are thought to drive corrosion through the formation of $CrF_3$, while extremely acidic solutions are also considered unfavorable. [9]

Table 2.3 Equilibrium concentrations of dissolved chromium upon contact of the pure metal with several fuel salt compositions. [9]

| Salt Composition (mol fraction) | | | [Cr] (ppm) | |
|---|---|---|---|---|
| NaF | $ZrF_4$ | $UF_4$ | 600°C | 800°C |
| 0.469 | 0.500 | 0.041 | 2300 | 2550 |
| 0.490 | 0.470 | 0.040 | 1700 | 2100 |
| 0.553 | 0.410 | 0.037 | 975 | 1050 |

The fission process also plays a non-negligible role in the corrosion performance of the system, as the sum of charges on all fission products is less than +4 per mol of uranium burned. [10] The excess fluorine drives an increase in the $UF_4$ to $UF_3$ ratio, creating a more oxidizing environment, and accelerating corrosion. However, this process can also be seen as having a benefit for plant operation, as solubility concerns associated with the $UF_3$ concentration are mitigated.

## 2.4 Additional Considerations

Although NaF is the only constituent that can be considered a commodity chemical, [8] emphasis was placed on de-risking the supply chain by not becoming reliant on enrichment processes that are not commercially available in the United States (e.g. $^{7}Li$, $^{37}Cl$, $^{235}U > 5\%$). By eliminating the option of $^{7}Li$, tritium production within these systems can be greatly reduced, and thus it was decided to also eliminate the possibility of using Be in order to devise a reactor that could operate with almost no tritium migration considerations.

In selecting a coolant salt, compatibility with the primary fuel salt was also considered. As the reactor has been designed to require next to no maintenance, having a system that would require minimal cleanup in the event of a leak or mixing of the two salts was a priority

# 3. Core Design

Figure 3.1 shows the radial cross-section of the TPX core layout, with Table 3.1 summarizing the materials and dimensions used. Sections 3.1 through 4 discuss the design process that has gone into this selection.

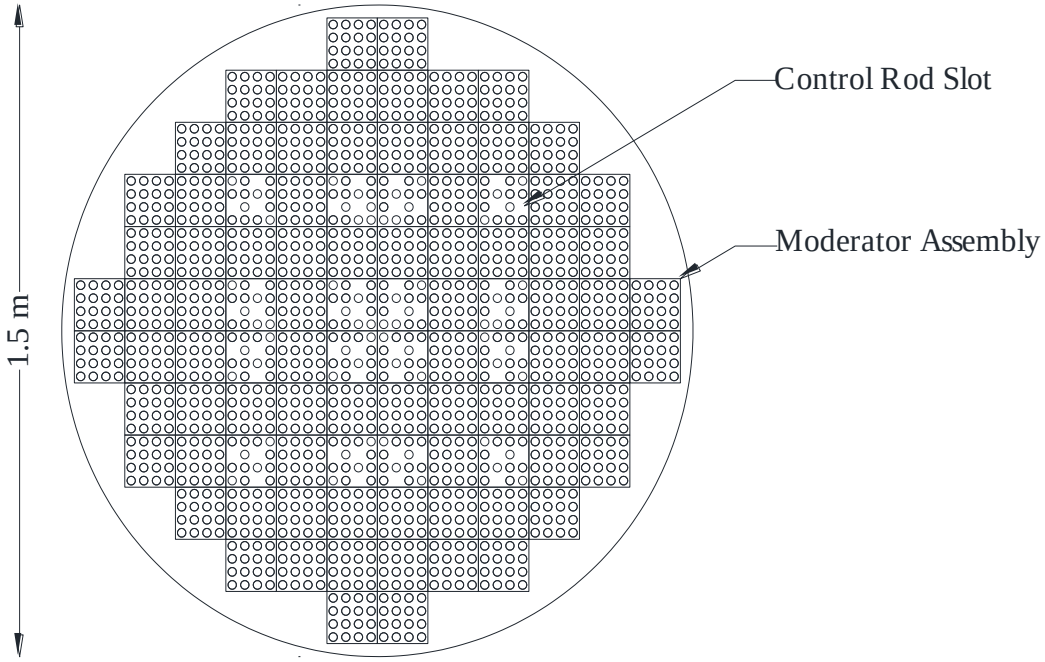


Figure 3.1 A radial core cross-section for one of the potential TPX core designs.

Table 3.1 A summary of the moderator and control rod materials and dimensions. The moderator cladding thickness is 0.001 m and the control rod cladding thickness is 0.002 m.

| | Moderator | Control | Cladding |
|---|---|---|---|
| Material | ZrH (δ – phase) | $Gd_2O_3$-$Al_2O_3$ | CVD SiC* |
| Radius (m) | 0.009 | 0.008 | --- |

*Monolithic silicon carbide

## 3.1 Moderator Rods

Metal hydrides are intriguing moderators because of their high hydrogen density and wide range of allowable operational temperatures. They have often been looked at for applications in which the weight and volume of a reactor needs to be minimized. [10] [11] Of the metal hydrides, δ – phase zirconium hydride is one of the most promising candidates, as it possesses good neutronic properties (low absorption cross-section, high hydrogen density) and shows adequate hydrogen stability when subject to a temperature gradient (Figure 3.2).

In order to be compatible in a fluoride salt environment, zirconium hydride must be clad so that it does not come in direct contact with the salt. [12] Potential claddings must be able to withstand high temperature and radiation environments, be compatible with fluoride salts themselves, have low absorption cross-sections, and act as a barrier for hydrogen diffusion in order to mitigate outgassing. Silicon carbide composites have garnered attention from the current light water industry as a possible alternative to Zircaloy, [14] however, the mechanical benefits that the composites possess over their monolithic counterparts are less desirable in the case of TPX. Monolithic CVD silicon carbide possesses higher thermal conductivity after irradiation, [15] has better corrosion performance in molten salts, [16] and there is greater experience in manufacturing compared to the SiC composites. [14] As a result, CVD SiC was chosen as the leading cladding candidate moving forward.

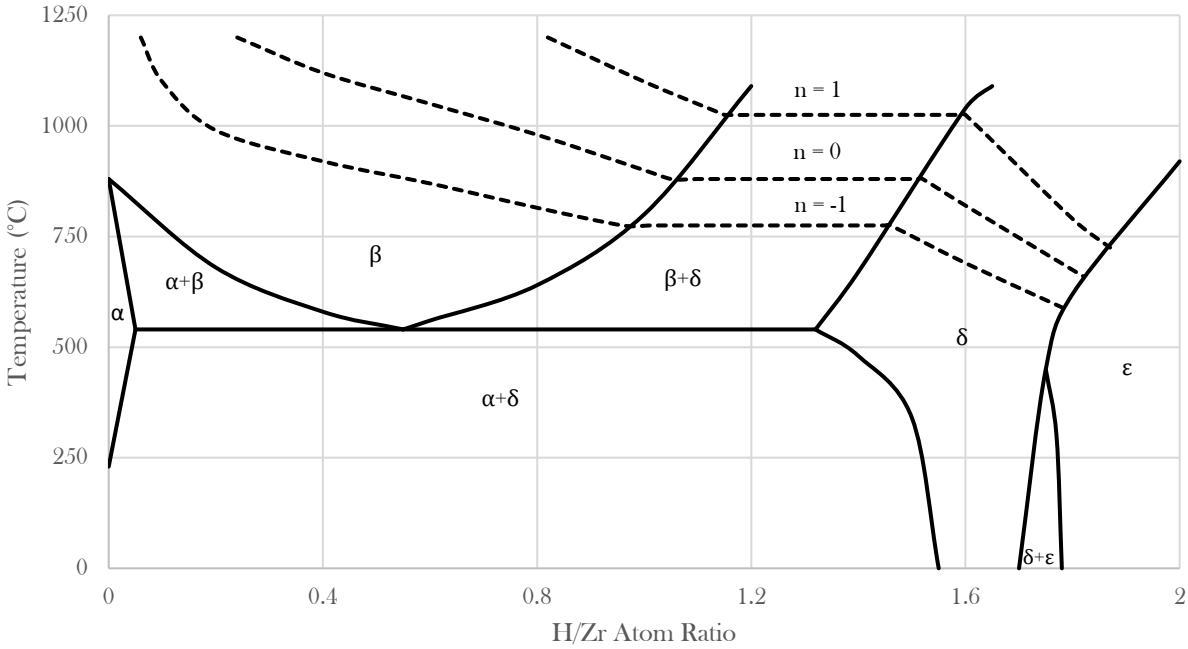


Figure 3.2 The zirconium hydride phase diagram overlaid with the partial pressure of hydrogen ($1 \cdot 10^n$ atm), with α indicating an hcp solid solution, β a bcc, δ an fcc, and ε an fct. [14]

The geometry of the rod itself was analyzed using the Monte Carlo neutronics software, Serpent 2.26, [15] varying the pitch and rod radius to find the optimal configuration. A SiC cladding thickness of 1 mm was selected as a conservative estimate for this analysis, and will be updated when more information on manufacturing is obtained.

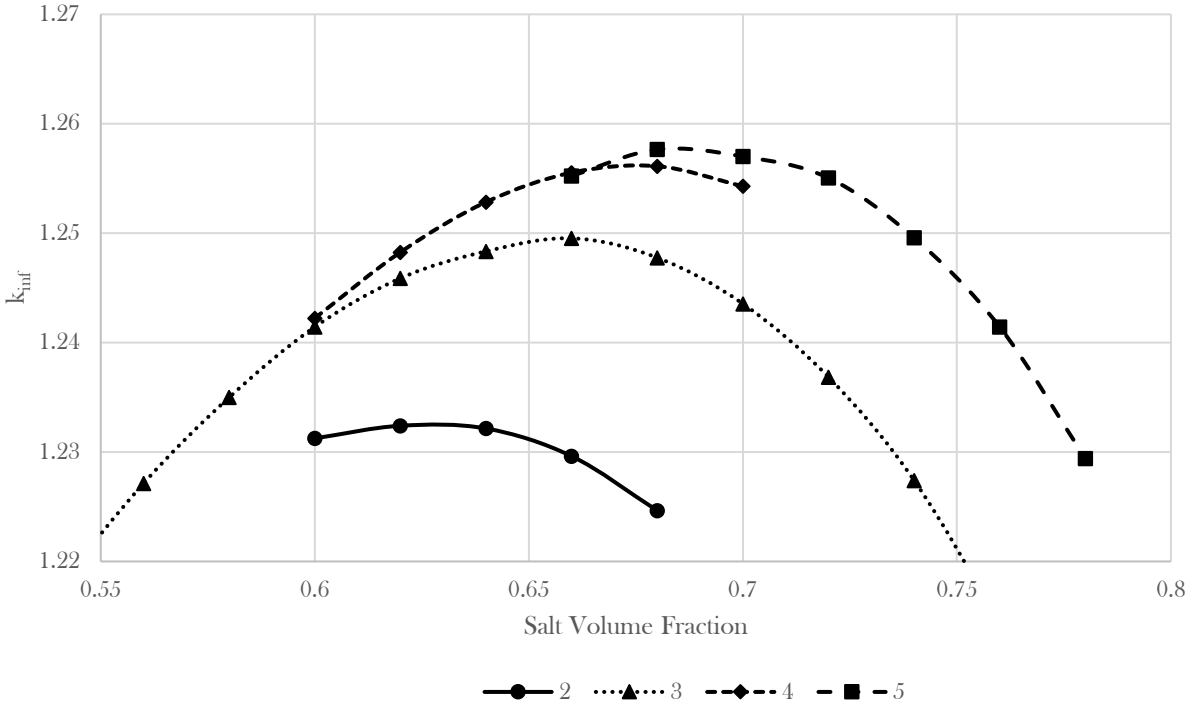


Figure 3.3 Infinite multiplication factor ($k_{inf}$) for a square pitch unit cell as a function of the salt volume fraction (SVF), with the legend indicating the pitch of the cell in cm.

As seen in Figure 3.3, although 4 and 5 cm pitch cells produced higher multiplication factors, the peak 3 cm geometry (0.66 SVF) was selected for the analysis moving forward. This choice was based around concerns over the manufacturing of large ZrH rods, [10] as well as limits in the rods' peak centerline temperature. [12]

## 3.2 Control Rods

Although several molten salt designs have proposed using fuel addition as a means of long term reactivity control, [19] TPX looks to avoid the added complications of online fuel processing and $^{235}U$ enrichments greater than 5% by using control rods. Although TPX operates near atmospheric pressure, limiting the number of vessel penetrations and subsequent drive mechanisms is still desirable to reduce overall cost, and therefore the design process was carried out with the goal of limiting the overall number of rods. Two candidate materials were explored: molybdenum hafnium carbide (MHC), a control element proposed as a potential candidate for FHRs, [20] and gadolinium aluminum oxide ($Gd_2O_3$-$Al_2O_3$), the control element used in the molten salt reactor experiment. [21] Despite requiring a cladding, gadolinium aluminum oxide was selected at this time as it requires less than half the number of MHC rods (48 vs 104).

## 3.3 Core Geometry

Selecting a core size is a balance between neutronic/material performance and cost. Larger cores have lower neutron leakage and reduced flux levels in the vessel and moderator, leading to longer maintenance and refueling intervals. However, the increased vessel radius, salt volume, and total number of moderator rods contributes to the overall plant cost.

Without reasonable economic estimates, the TPX core size was chosen by selecting the smallest geometry capable of achieving and maintaining criticality (Figure 3.4 & Figure 3.5). Four-by-four rod assemblies (Figure 3.1) were defined for the full core analysis and act solely as a place holder as no optimization into assembly size has been performed.

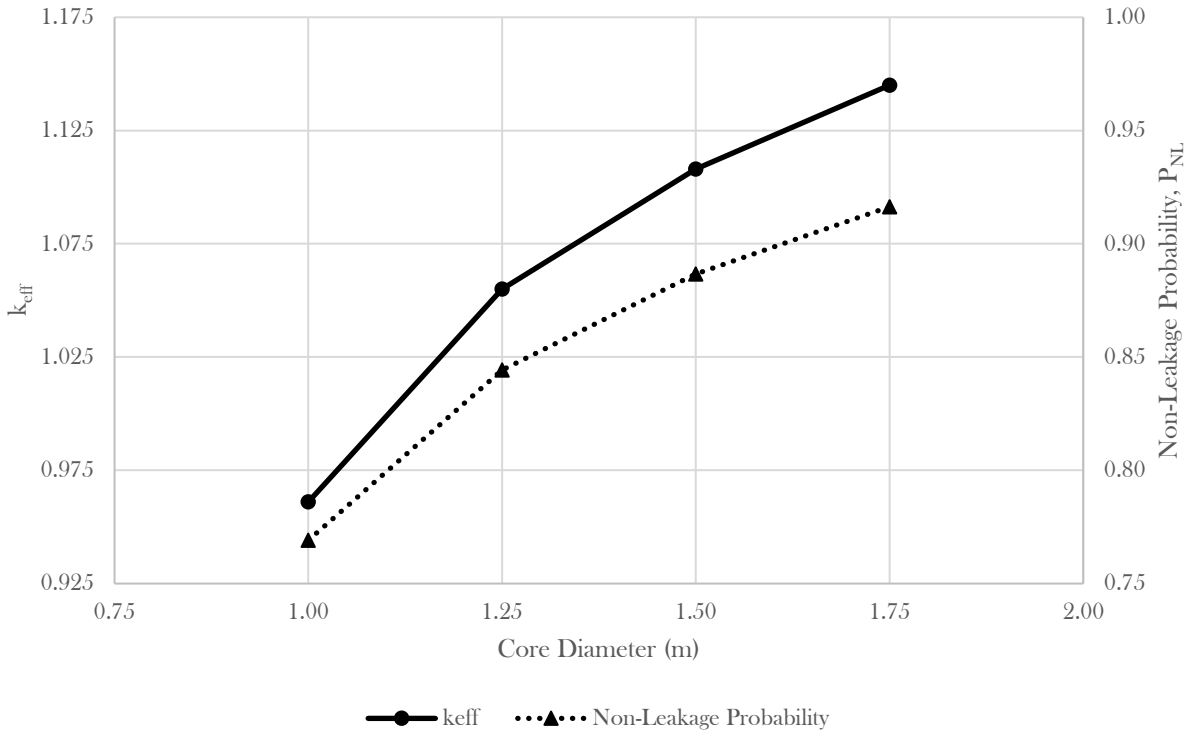


Figure 3.4 The effective multiplication factor ($k_{eff}$) and corresponding non-leakage probability ($P_{NL}$) as a function of core diameter. The core diameter does not take into account the thickness or presence of a vessel material.

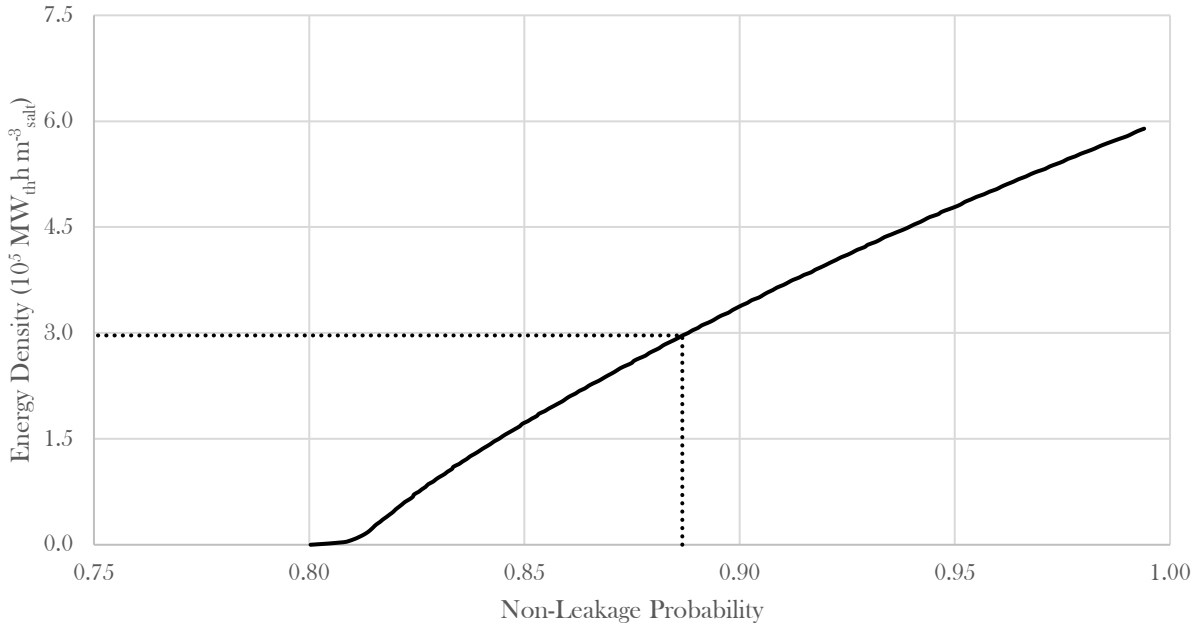


Figure 3.5 Energy per unit volume of fuel salt as a function of the neutron leakage in the core. The dotted line represents the expected leakage of the geometry displayed in Figure 3.1 (1.5m core diameter).

## 3.4 Safety Performance

Although the emergency cooling requirements for liquid fueled systems are simplified as a result of the convective nature of the fluid, the reactor must still be able to be controlled and shutdown effectively. Table 3.2 illustrates the strong negative reactivity coefficients that the system possesses, allowing for further inherent stability and safety.

$$Reactivtiy\ Coefecient = \frac{k_2 - k_1}{k_2 k_1 (T_2 - T_1)} \qquad \text{Eq 3.1}$$

Table 3.2 Reactivity coefficients (pcm $K^{-1}$) for two different TPX core configurations; control rods in (CR In) and control rods out (CR out). Three coefficients were calculated; fuel density (F-Density), fuel temperature (F-Temp) and moderator temperature (M-Temp).

| Core Configuration | Temperature Range (K) | F-Density | F-Temp | M-Temp |
|---|---|---|---|---|
| CR In | 600 to 900 | -6.02E-05 | -3.48E-05 | -5.39E-05 |
| | 900 to 1200 | -6.76E-05 | -3.14E-05 | -5.35E-05 |
| CR out | 600 to 900 | -2.29E-05 | -2.83E-05 | -1.43E-05 |
| | 900 to 1200 | -2.72E-05 | -2.50E-05 | -1.62E-05 |

As simulations were run with a beginning of life fuel composition, the control rods out (CR out) configuration acts as a conservative estimate of the coefficients that will exist at the end of life (as the introduction of fission products and transuranics should decrease the values further). [22]

# 4. Heat Transfer and Conversion

The TPX power system is designed for simplicity and ease of operation. Both the primary and secondary salt loops can function on natural circulation, eliminating the need for any molten salt pump components, increasing passive safety, and dampening any operational or unplanned thermal transients. Section 4.1 gives an overview of this heat transfer system, section 4.2 explains the operational principle of natural circulation within the primary loop, section 4.3 gives an overview of heat exchanger design and selection, and section 4.4 describes the geometry optimization process that produces functional designs.

## 4.1 Power Cycle & Regulation

The primary loop transfers heat via natural circulation to the secondary cycle through the integral heat exchanger between the riser and vessel wall. The secondary loop is connected by radiator to a tertiary power cycle that consists of an open-air Brayton cycle. Operators can control core power and temperature change through the primary loop by regulating turbine load. Thermal hydraulic operation is summarized in Table 4.1.

Table 4.1 Summary of the TPX heat loops and power cycle. Power range for the Primary system is 5–25 $MW_{th}$.

| | Operational Principle | Working Fluid | Temperature Range |
|---|---|---|---|
| Primary | Natural Circulation | $NaF\text{-}ZrF_4\text{-}UF_4$ | 605 – 670* |
| Secondary | Forced (Pumped) Circulation | $NaF\text{-}ZrF_4$** | 550 – 660 |
| Tertiary | Open Brayton Cycle | Air | 650*** |

* The minimum operational temperature is selected to provide sufficient margin against salt freezing, while the maximum is limited to reduce creep in structural materials and hydrogen outgassing in the moderator.
** Secondary coolant could also be helium gas in a double walled heat exchanger configuration.
*** Turbine intake maximum temperature.

## 4.2 Primary Loop Natural Circulation

The range of acceptable core power levels is limited by the ability to remove heat through natural circulation. In general, the onset of natural circulation occurs when the Rayleigh number is sufficiently high that buoyancy-driven flow (free convection) can occur. [16] Circulation of this flow is maintained in the primary loop if the flow generated by natural circulation forces can overcome the frictional losses the flow endures around the loop.

Through conservation of energy, conservation of momentum, and a few reasonable assumptions, the relationship between primary loop power, natural convection, and geometry can be simplified to a single equation describing achievable fluid velocity in the core (Eq 4.1). [17]

Assumptions:

- 1-D flow
- Boussinesq approximation
- Incompressible working fluid
- Core inlet temperature ($T_c$) is constant (600 °C)
- Power generated in the core (Q) is equal to that removed by the heat exchanger

Achievable core velocity ($u$):

$$u = \left( \frac{\beta \, Q \, L_{th} \, g}{\rho \, A_{core} \, c_p \, \Pi} \right)^{\frac{1}{3}} \qquad \text{Eq 4.1}$$

In determining the operation power/temperature range under natural circulation, the achievable core velocity can be compared to the minimum required core velocity, $v$, (determined from conservation of energy alone). This is the required velocity to remove some amount of core power at a given temperature change across the core.

Minimum required core velocity ($v$):

$$v = \frac{\mathrm{Q}}{\Delta \mathrm{T}_{\mathrm{core}}\ \mathrm{c_p}\ \rho\ \mathrm{A}_{\mathrm{core}}} \qquad \text{Eq 4.2}$$

The power, Q, and temperature change, ΔT, are functions of the heat transfer design and controlled by the tertiary cycle. Characteristic length of convection (distance from midplane of core to midplane of heat exchanger), $L_{th}$, and loop resistance, Π, are geometry-dependent parameters, determined by the vessel and internal design. The vessel and heat transfer designs are interrelated through the heat exchanger geometry. All other parameters are thermophysical properties of the salt or determined by the reactor physics.

The dimensionless loop resistance, Π, accounts for flow resistance which inhibits natural circulation due to friction, area change, and other K-loss contributors. It is represented by Eq 4.3. For additional details, see Appendix B.

$$\Pi = \sum_{i=1}^{N} \left[ \frac{1}{2} \left( \frac{f_i L_i}{D_h} + K_i \right) \left( \frac{A_{core}}{A_i} \right)^2 \right] \qquad \text{Eq 4.3}$$

Neutrons and photons that leak from the core and deposit in the downcomer also act as an impediment to natural circulation, as the added heat generation attempts to raise the temperature of the salt in the downcomer region. In order to take into account this phenomenon, a counteracting mass flow rate was calculated based on the power generation in the downcomer region (Appendix D). Eq. 4.4 defines the negative velocity contribution used in the model.

$$u^{-} = \left( \frac{\beta\ \mathrm{Q}_{DC}\ \mathrm{L_{th}}\ \mathrm{g}}{\rho\ \mathrm{A_{DC}} \mathrm{c_p}\ \Pi} \right)^{\frac{1}{3}} \cdot \left( \frac{\mathrm{A_{DC}}}{\mathrm{A_{core}}} \right) \qquad \text{Eq 4.4}$$

## 4.3 Heat Exchanger Design

Straight tube and helical coil heat exchanger designs were also considered within the integral vessel. To compare the two heat exchanger designs, the vessel diameter was held fixed, and the area of the annular compartment housing the heat exchanger was varied by adjusting the riser radius. The straight tube and helical coil heat exchangers were both arranged in a square pitch, resulting in approximately the same heat transfer area (tube surface area) for a given compartment size. A view of tube placement in the heat exchanger compartment is shown below in Figure 4.1.

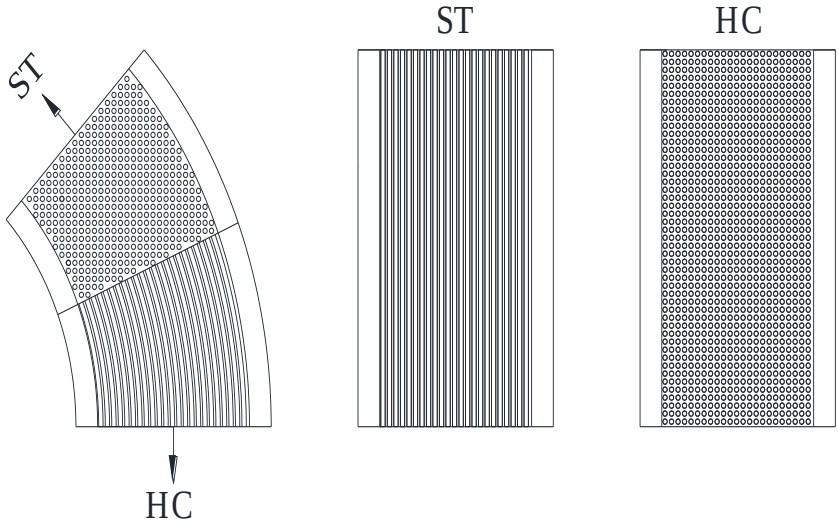


Figure 4.1 Radial [left] and axial [center & right] cutaways for tube placement in helical coil and straight tube heat exchangers with square pitches.

The helical coil heat exchanger is preferred due to its higher heat removal capacity given the same channel size. This holds true for any channel size, as shown in Figure 4.2, primarily due to the higher heat transfer coefficient. The frictional losses are higher in a helical coil geometry, but the heat transfer advantage vastly outweighs the flow loss disadvantage.

A double-tube heat exchanger could also be used to eliminate the need for a larger secondary loop. In this configuration, the gap between inner and outer tubes would be filled with helium, while compressed air would travel inside the innermost layer of the tubes to transfer heat from the primary. This presents additional manufacturing and safety challenges, but may ultimately reduce cost as it removes the need for a secondary salt.

Additional details on the heat transfer coefficients and frictional loss calculations can be found in Appendix B.

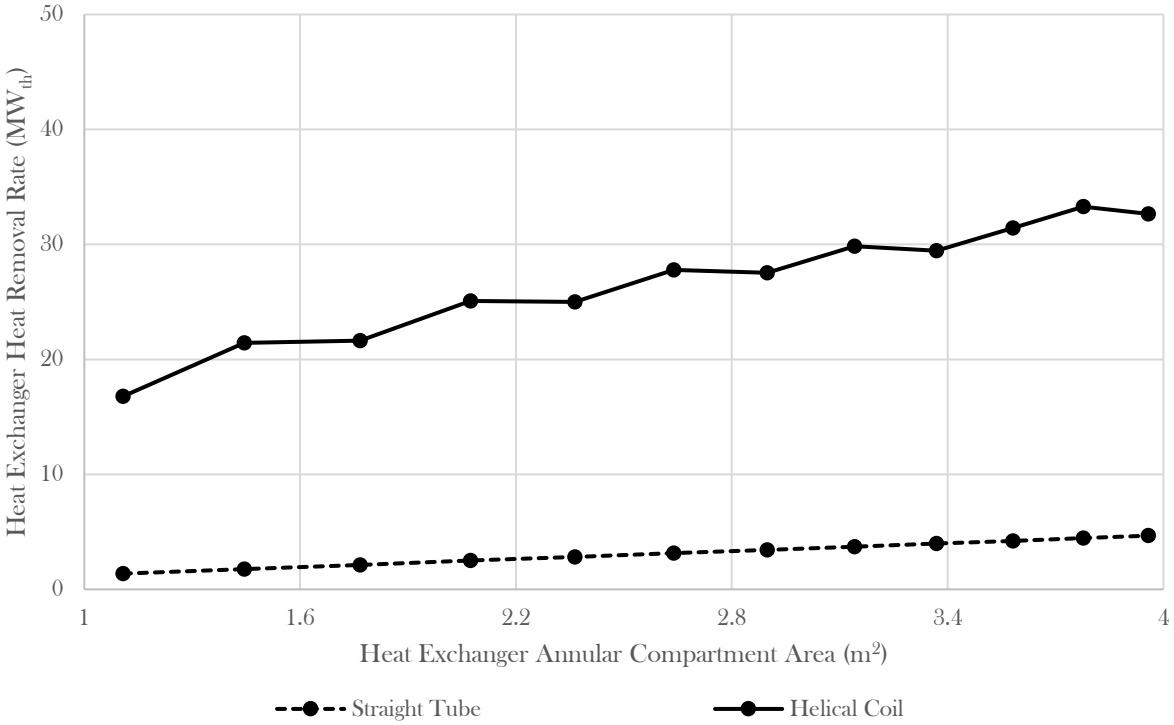


Figure 4.2 Heat exchanger heat removal capacity ($Q_{HX}$) for straight tube and helical coil heat exchangers as a function of exchanger region annulus area with a heat exchanger temperature difference of 10 °C and tube pitch of 11 mm.

## 4.4 Geometry Optimization

A robust scoping tool and optimization routine was developed to evaluate integral vessel geometries, with scoping being performed by varying the following parameters:

- Heat exchanger bulk fuel salt and tube surface temperature difference, $\Delta T_{HX}$
- Heat exchanger tube pitch, p
- Heat exchanger pipe radius, $R_{HxPipes}$
- Riser radius, $R_R$
- Riser height, $H_R$
- Heat exchanger channel thickness, $T_{HX}$ (the annulus between the vessel and inner barrel)
- Downcomer thickness, $T_{DC}$ (the unoccupied annulus below the heat exchanger)
- Thickness of the upper gap, $T_{UG}$

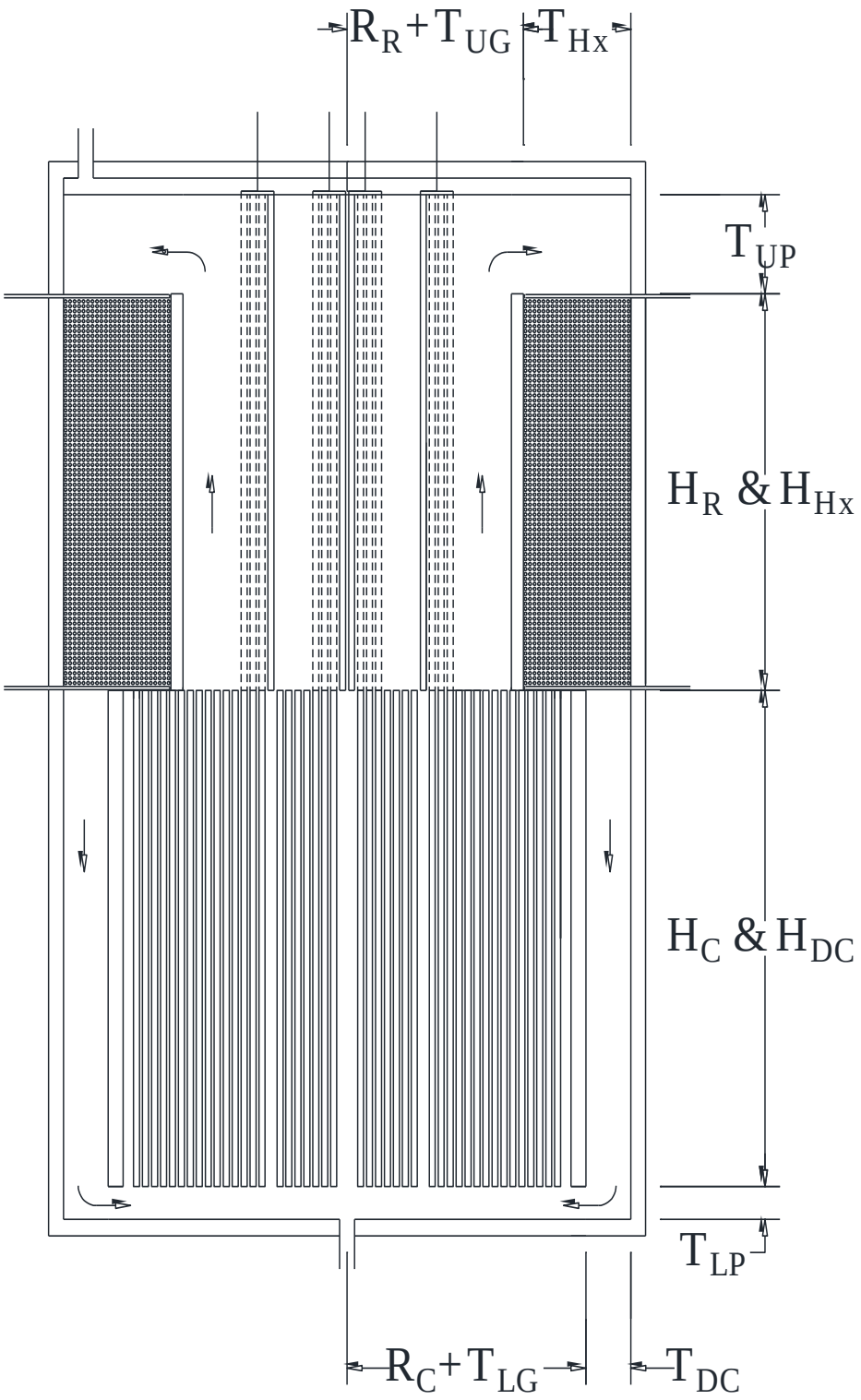


Figure 4.3 An axial cross-section depicting the relevant geometrical parameters for optimization.

During the scoping phase, the optimization routine also required that geometries satisfy a series of flexibility/operational requirements:

(1) $u \geq v$

Achievable core velocity (u) exceeds minimum required core velocity (v). This ensures natural circulation results in sufficiently high flow rates for all heat removal during operation.

(2) $\frac{V_{salt} \cdot \tau}{Q} \geq 10\ years$

The salt volume ($V_{salt}$) must be sufficient for at least 10 years of operation without refueling at the highest core power level (Q). The lifetime constant ($\tau$) is a function of the achievable burnup, which is partially dependent on the downcomer radius.

$$\tau = -20.31 \cdot T_{DC}^6 + 80.63 \cdot T_{DC}^5 - 127.19 \cdot T_{DC}^4 + 101.44 \cdot T_{DC}^3 - 42.94 \cdot T_{DC}^2 + 9.14 \cdot T_{DC} + 37.69 \quad \text{Eq 4.5}$$

(3) $H_{upper\ vessel} = 1.5\ m$

The upper vessel interior height (riser, upper plenum, and gas gap) must be tall enough to accommodate full control rod withdrawal and drive shaft connectors in order to reduce vessel penetrations. Taller geometries were not considered at this time based on the resulting increased excavation requirements, however, this criterion will be modified when more economic information is obtained.

(4) $Q_{HX} \geq Q$

The power removed by the heat exchanger must meet or exceed the maximum core power. This must also take into account heat exchanger fouling.

(5) $D_{vessel} \leq 2.6\ m$

The overall vessel diameter was limited to 2.6m (including the vessel itself) to fit within standard road-shipping limits. It should be noted that wider vessels allow for more salt and thus a higher power. Wider vessels also increase manufacturing challenges and initial cost.

(6) $H_{DC} = H_{core} = 1.5\ m$

The base of the heat exchanger was also set to be above the core to minimize activation and material damage. This requirement means the downcomer height must be equal to the height of the core.

(7) $T_{mod} = 800°C$

In order to limit outgassing of hydrogen from the moderator, the centerline temperature of the hottest rod has been restricted to 800°C. This restriction determines the temperature rise across the core ($\Delta T_{core}$) as a function of power level (Q), with more details being provided in appendix B and C.

$$\Delta T_{core} = 7.8418 \cdot \ln(Q) + 38.7281 \quad \text{Eq 4.6}$$

Upon satisfying these requirements, the results were then sorted based on a levelized cost ($L_C$), calculated using the total cost of the system and maximum power level (Q). As many aspects of the design do not yet have accurate cost data associated with them, an initial estimate has been devised using approximations for some of the larger components: Moderator rod cost ($C_M$), fuel salt cost ($C_F$), vessel cost ($C_V$), heat exchanger cost ($C_{HX}$), and balance of plant cost ($C_{BP}$). For more information on cost analysis see Appendix E.

$$L_C = \frac{C_M + C_F + C_V + C_{HX} + C_{BP}}{Q} \quad \text{Eq 4.7}$$

# 5. Operations

The TPX reactor is designed for long periods of continuous power operation without maintenance or refueling, and completely passive emergency safety.

The operational modes, further described in section 5.1, include:

- Fuel Loading
- Startup
- Power Generation (Normal Operation)
- Shutdown
- Maintenance & Refill
- Refuel
- Off-Normal and Emergency Operation

Additional operational procedures and designs are discussed in section 5.3.

## 5.2 Conceptual Plant Operating Procedures

### 5.2.1 Fuel Loading

Frozen fuel bricks are loaded into the clean salt fuel tank via the brick addition port. This can occur at the plant or at a central facility if the mobile refueling option is selected. To remove volatiles and oxygen impurities, a vacuum is applied to the tank (via lines along valves 110-113). The bricks are heated to a temperature slightly below the melting point of the salt via heaters wrapped around the fill tank. The vacuum pump is then shut off and the atmosphere is replaced with helium (via lines along valves 114-116 & 110). Salt is heated further to melt it. Vessel heaters are turned on to prepare it to receive salt. Valves between the core fuel inlet and fill tank (100, 101, & 105) are opened, allowing molten salt to flow into the core along the fill line, driven by gravity and/or helium gas backpressure. Once all fuel has been transferred to the vessel, the valves are closed and the reactor is ready for startup.

### 5.2.2 Startup

During startup, control rods are withdrawn, and the reactor begins to generate heat. The heat removal is ramped up via compressor-turbine actuation, until a steady-state minimum operational power has been reached. At 5 MWth, the reactor is considered to be in Power Generation mode.

### 5.2.3 Power Generation (Normal Operation)

Once the reactor has reached 5 MWth, power regulation up to the peak thermal power is controlled primarily by turbine demand. Over the course of depletion, control rods are adjusted to maintain criticality.

During operation, gaseous fission products accumulate in the upper vessel space above the upper plenum, traveling through an outlet pipe and an open valve (106) into the drain/off-gas expansion tank. The large capacity tanks act as a hold-up volume for fission product gases. The tank volume is sufficiently large that it can accommodate all gaseous fission products generated over the course of reactor life without ever exceeding atmospheric pressure.

Anticipated operational transients of the largest severity are induced by power changes and accommodated by design, so other transients are lumped either in emergency operations or assumed to be covered by the ranges of normal systems operation.

### 5.2.4 Shutdown

The reactor is shut down by full insertion of all control rods, or by insertion of shutdown rod, thereby ceasing the fission process. Decay heat is removed during normal shutdown operation by continued compressor-turbine actuation. Once a low temperature is achieved, the compressor-turbine system is decoupled by regulated opening of the secondary heat exchanger ventilation gates. Hot shutdown is maintained indefinitely in this mode until salt is drained or the reactor is restarted.

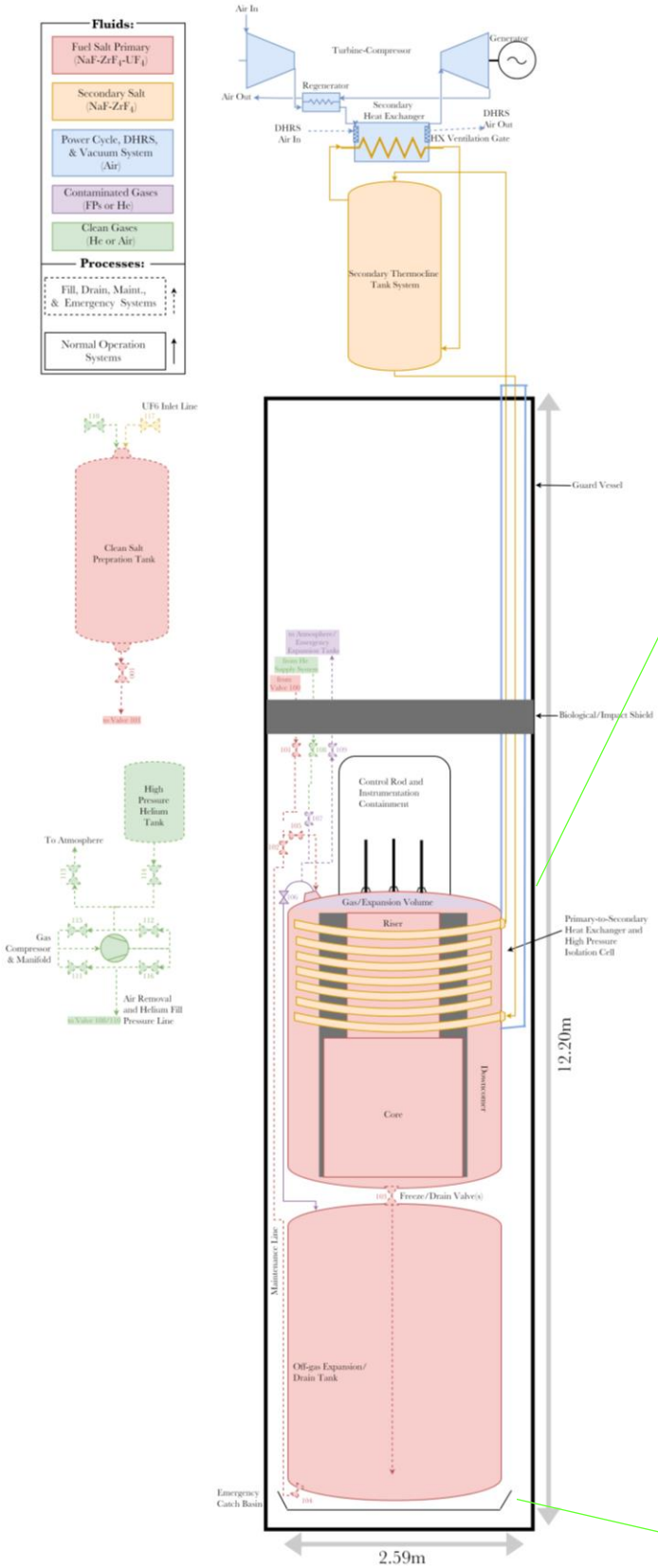


Figure 5.1 Process flow diagram overview of the TPX system integration and layout.

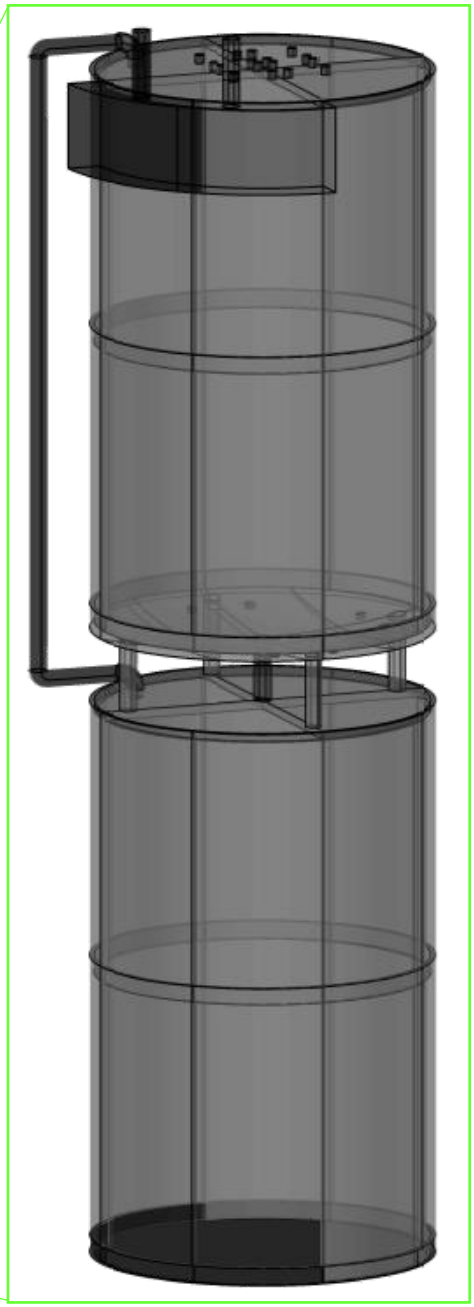

Figure 5.2 Render of TPX Primary

### 5.2.5 Off-Normal & Emergency Operations

The reactivity of the system is controlled by a number of natural phenomena (all reactivity coefficients are negative) and physical devices (control rods and shutdown rod). In the event these fail, the drain tank allows the fuel salt to drain from the reactor into a non-critical configuration and remove decay heat. This drain tank also serves as an expansion volume for fission gases produced over the life of the reactor. While TPX does not produce significant quantities of tritium, gases like Xenon and Krypton may come out of salt solution and accumulate in the cover gas region. The drain tank is designed to provide sufficient expansion volume to maintain atmospheric pressure throughout the primary system for the entire fuel cycle of TPX.

As there are no pumps in the primary loop, design basis events/emergency scenarios involve a loss of flow in the secondary/tertiary or a break within the fuel or coolant salt systems. All emergency operations are expected to follow a reactor trip (shutdown configuration insertion of the control + shutdown rods). The decay heat is expected to decline exponentially starting at ~6.5% of peak operational power as shown in Figure 5.5.

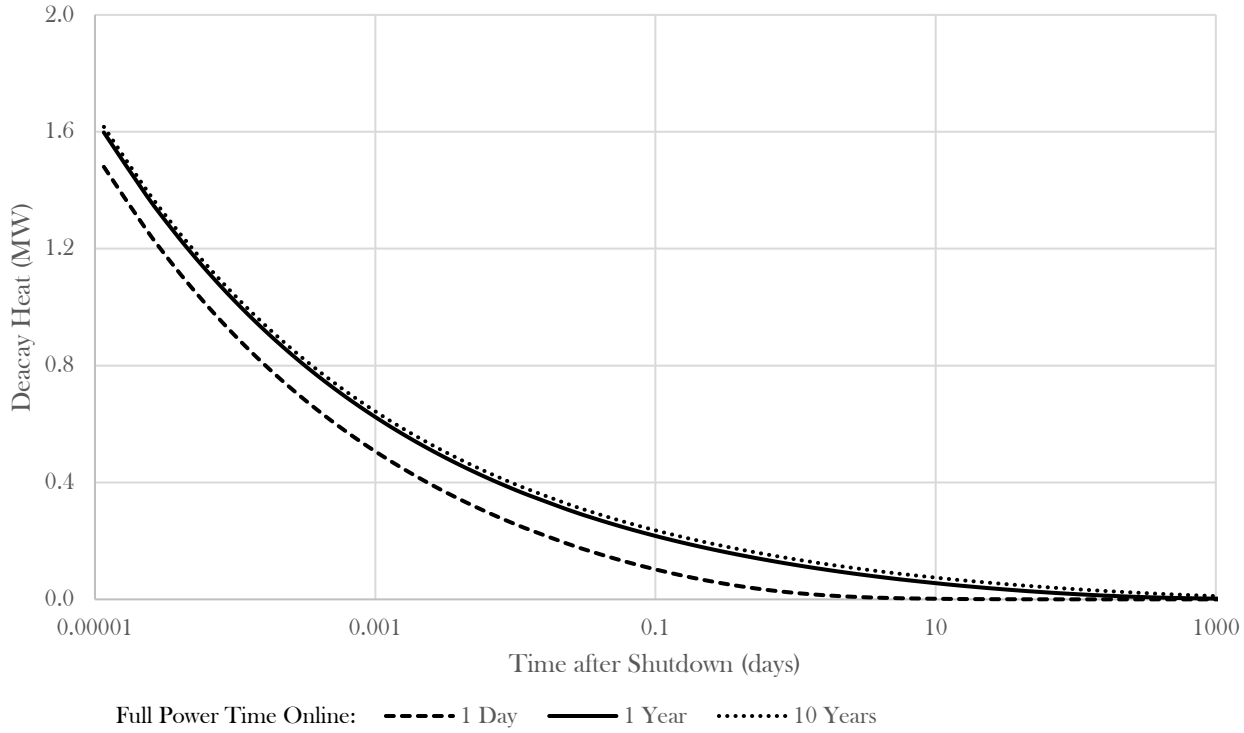


Figure 5.3 Decay heat load after shutdown for a range of full-power (25 $MW_{th}$) operation times.

Because the compressor is driven by the turbine, a loss of offsite power (LOOP) or other disconnection from grid power does not inhibit standard operation heat removal via the power cycle, and the generator shaft could continue to provide power to auxiliary systems as necessary as the reactor coasts down. For this reason, a LOOP is treated as analogous to normal shutdown.

Loss of tertiary cooling (e.g., turbine malfunction), is accounted for by the secondary heat exchanger ventilation gates. These gates are on electromagnetic actuators, powered by the turbine-generator. On loss of turbine functionality, these gates drop open, allowing the system to cool via natural convection through the secondary heat exchanger.

Secondary loop rupture is accounted for through the design of the containment shell. Normally the shell is filled with inert gas and acting as an insulator for the primary system. When the secondary loop breaks, the salt within drains into

the shell space, allowing increased heat transfer by both conduction and radiation from the reactor vessel to the shell, allowing the earth to serve as the ultimate heat sink.

Primary vessel breaks are held within the containment shell. The increase in surface area and increased heat transfer to earth allows for more effective passive to-earth cooling.

Rupture of the primary involves no driving pressure, and the entire primary fits in the shipping container containment, the exterior of which will be a layer of concrete, limiting material release. The primary system would eventually mix with the argon or helium cover gas but not be propagated out without additional containment and concrete shell breaks. This scenario would be quickly detected by monitoring equipment.

#### 5.2.6 Maintenance & Refill

In the unlikely and undesirable event maintenance must be performed on-site, the reactor can be prematurely drained. From shutdown, the used salt drain line is thawed opened (103). If necessary, valve (106) is closed, valves (107) and (108) are opened, and fuel is forced into the used salt tank by helium backpressure. The salt is maintained above 200 °C in the drain tank (typically via decay heat) in order to inhibit the effects of radiolysis during maintenance. Once maintenance is complete, the freeze valve (103) is sealed, salt is heated to operational temperatures, downstream valves open (102, 104, 105, & 106), and the salt is reloaded through the maintenance line (valves 104-102-105) via helium backpressure (via 108-107-106, with gas outlet of primary sealed).

It should be noted that, the highest turbine reliabilities are around 99.4%, meaning some maintenance will need to be performed on them during the operational life of the reactor (~3 weeks of downtime for a 10-year cycle). This maintenance may or may not affect the reactor itself if the configuration of the plant allows for the reactor to be maintained at low power during turbine maintenance.

### 5.3 Additional Procedures and Plant Designs

#### 5.3.1 Secondary Salt Loading

Secondary salt is currently designed as a thermocline tank(s) system, which provides a large thermal reservoir and buffer to tertiary transients. The salt is prepared and loaded much the same way fuel salt is prepared: heated in brick form, volatiles removed by vacuum, melted, and loaded into the tank via gravity and/or helium backpressure. It is not anticipated that the secondary salt loop will be drained or refilled during operation; however, an additional pipe-valve connection could be provided near a low elevation for draining.

#### 5.3.2 Decommissioning

Decommissioning has not be addressed in depth as the federal policy and procedure for nuclear used fuel disposal may differ from the current status-quo when the reactors are deployed. The entire primary is contained within the hardened shipping container and used fuel could be transported inside the drain tank to a reprocessing or disposal site easily. After sitting for an acceptable amount of time to reduce decay heat to negligible levels (primarily determined by desired temperatures for transporting salt) and fission product gases to background levels, the fission product gases are vented to remove any pressure in the vessel during transport. The plant itself would likely be decommissioned using SAFESTOR, where the reactor vessel is allowed to sit in place until it has reduced in radioactive "heat" similar to LWR components. [19]

#### 5.3.3 Multiple Turbine Configuration

A single turbine may not be able to operate at the full range of viable power levels. Therefore, a combination of turbines could be couple with a single unit to provide ranges of power accommodating end-user needs. For example, a small variable-load turbine could be coupled with a single turbine closely approximating the daily average electricity use of the user, with the variable turbine meeting peak demand loads. A similar arrangement could apply to co-generation. Multiple turbines could also be used if on-line maintenance is desired.

# References


[1] M. Rosenthal , P. Kasten and R. Briggs, "Molten-salt reactors history, status, and potential.," Oak Ridge National Laboratory, 1969.

[2] Defense Science Board, "Task force on energy systems for forward/remote operating bases," Department of Defence, 2016.

[3] W. R. Grimes, "Molten-salt reactor chemistry," Oak Ridge National Lab, 1969.

[4] R. Thoma, "Phase diagrams of nuclear reactor materials," Oak Ridge National Laboratory, 1959.

[5] K. Sense, C. Alexander, R. Bowman and R. Filbert, "Vapor pressure and derived information of the sodium fluoride-zirocnium fluoride system. Description of a method for the determination of molecular complexes present in the vapor phase.," Journal of Physical Chemistry, 1957.

[6] W. Jordan, S. Cromer and A. Miller, "Aircraft nuclear propulsion project quarterly progress report for period ending september 10, 1956," Oak Ridge National Lab, 1956.

[7] W. Jordan, S. Cromer and A. Miller, "Aircraft nuclear propulsion project quarterly progress report for period ending December 31, 1956," Oak Ridge National Laboratory, 1957.

[8] D. Williams, L. Toth and K. Clarno, "Assessment of candidate molten salt coolants for the advanced high-temperature reactor (AHTR)," Oak Ridge National Laboratory, 2006.

[9] D. Williams and L. Toth, "Chemical considerations for the selction of he coolant for the advanced high-temperature reactor," Oak Ridge National Laboratory, 2005.

[10] C. Baes, "The chemistry and thermodynamics of molten salt reactor fuels," Journal of Nuclear Materials, 1974.

[11] J. Vetrano, "Hydrides as neutron neutron moderator and reflector materials," Nuclear Engineering and Design, 1970.

[12] R. Harde and K. Stohr, "A sodium-cooled power reactor experiment employing zirconium-hydride moderator," 1964.

[13] W. Jordan, S. Cromer, A. Miller and A. Savolaninen, "Aircarft nuclear proplusion project quarterly progress report for period ending december 10, 1955," Oak Ridge National Lab, 1956.

[14] W. Kim, D. Kim and J. Park, "Fabrication and material issues for the application of SiC composites to LWR fuel cladding," Korea Atomic Energy Research Institute, 2013.

[15] Y. Katoh, T. Nozawa, L. Snead and H. Tanigawa, "Stability of SiC and its composites at high neutron fluence," Journal of Nuclear Materials, 2011.

[16] C. Forsberg, L. Hu, P. Peterson and K. Sridharan, "Fluoride-salt-cooled high-temperature reactor (FHR) for power and process heat," Advanced Nuclear Power Report Series, 2014.

[17] D. Olander, E. Greenspan and H. Garkisch, "Uranium-zirconium hydride fuel properties," Nuclear Engineering and Design, 2009.

[18] J. Leppanen, "Development of a new monte carlo reactor physics code," Helsinki University of Technology, 2007.

[19] R. Robertson, "Conceptual design study of a single-fluid molten salt breeder reactor," Oak Ridge National Laboratory, 1971.

[20] University of Wisconsin Madison, "Materials, activation, tritium and transport (MATT) group: status and path forward," Nuclear Energy University Program, 2017.

[21] G. Tolson and A. Taboada, "MSRE control elements: manufacture, inspection, drawings, and specifications," Oak Ridge National Laboratory, 1967.

[22] B. Betzler, S. Robertson, E. Davidson, J. Powers, A. Worrall, L. Dewan and Massie M, "Assessment of the neutronic and fuel cycle performance of the Transatomic Power molten salt reactor design," Oak Ridge National Laboratory, 2017.

[23] F. P. Incropera, D. P. Dewitt and et al, Fundamentals of Heat and Mass Transfer, 7th ed., Jefferson City: John Wiley & Sons, Inc., 2011.

[24] International Atomic Energy Agency, "Natural circulation in water cooled nuclear power plants," IAEA, Vienna, 2005.

[25] United States Nuclear Regulatory Commission, "10 CRF Appendix I to Part 50—Numerical Guides for Design Objectives and Limiting Conditions for Operation to Meet the Criterion "As Low as is Reasonably Achievable" for Radioactive Material in Light-Water-Cooled Nuclear Power Reactor Effluents," US NRC, 2015 2 December. [Online]. Available: https://www.nrc.gov/reading-rm/doc-collections/cfr/part050/part050-appi.html. [Accessed 17 May 2017].

[26] United States Nuclear Regulatory Commission, "Backgrounder on Decommissioning Nuclear Power Plants," US NRC, 14 May 2015. [Online]. Available: https://www.nrc.gov/reading-rm/doc-collections/fact-sheets/decommissioning.html. [Accessed 17 May 2017].

[27] W. Grimes, "Reactor chemistry division annual progress report for period ending december 31st," Oak Ridge National Laboratory, 1965.

[28] S. Cohen, W. Powers and N. Greene, "A physical property summary for ANP fluoride mixtures," Oak Ridge National Lab, 1956.

[29] M. Hossain, M. Kassaee, S. Jeter and A. Teja, "A new model for the thermal conductivity of molten salts," Int J Thermophys, 20114.

[30] I. Idel'chik, Handbook of Hydraulic Resistance, Washington, D.C.: US NRC (Reprint), 1966.

[31] J. Coates and B. S. Pressburg, "Heat Transfer to Moving Fluids," *Chemical Engineering,* pp. 67-72, 1959.

[32] D. Q. Kern, "Process Heat Transfer," New York, McGraw-Hill, 1950, pp. 103, 137, 549, 721, 834.

[33] wise-uranium.org, "5% U235," 2017.

[34] Arc Applications Inc, "Incoloy 800H Ni 201 composite," 2017.

[35] U.S Department of Energy, "Gast Turbines - Combined heat and power technology fact sheet series," 2016.

[36] C. Deck, H. Khalifa, B. Sammuli, T. Hilsabeck and C. Back, "Fabrication of SiC-SiC composites for fuel caldding in advanced reactor designs," Progress in Nuclear Energy, 2012.

[37] R. Thoma, "Phase diagrams of nuclear reactor materials," Oak Ridge National Laboratory, 1959.

[38] W. Gambill, "Prediction of the thermal conductivity of fused salts," Oak Ridge National Lab, 1956.

[39] United States Nuclear Regulatory Commission, "Glossary: Shutdown Margin," US NRC, 10 April 2017. [Online]. Available: https://www.nrc.gov/reading-rm/basic-ref/glossary/shutdown-margin.html. [Accessed 18 May 2017].

# Appendix A. Fuel Salt Property Determination

## A.1. Density

The salt's density, ρ (g $cm^{-3}$), and thermal expansion coefficient, β ($°C^{-1}$), have been calculated through an additive molar volume method (Eq A.1) based on the data provided in Table A.1, with $X_i$ being the mol fraction of each constituent, $M_i$ the molar mass, and $V_i$ the molar volume.

$$\rho = \frac{\Sigma X_i M_i}{\Sigma X_i V_i} \qquad \text{Eq A.1}$$

Table A.1 Experimental values for molar volumes of the Fluorides comprising the NaF-$ZrF_4$-$UF_4$ system. [20]

| | Molar Volume, $V_i$ ($cm^3$ $mol^{-1}$) | | |
|---|---|---|---|
| Temperature (°C) | NaF | $ZrF_4$ | $UF_4$ |
| 600 | 19.08 | 47 | 45.5 |
| 800 | 20.20 | 50 | 46.7 |

## A.2. Viscosity

The viscosity of a molten salt does not currently have a predictive correlation that is widely used in the literature. However, by plotting the data that is present for the NaF-$ZrF_4$-$UF_4$ system as a function of the molar mass of each composition (Figure A.1) a simple linear trend can be observed.

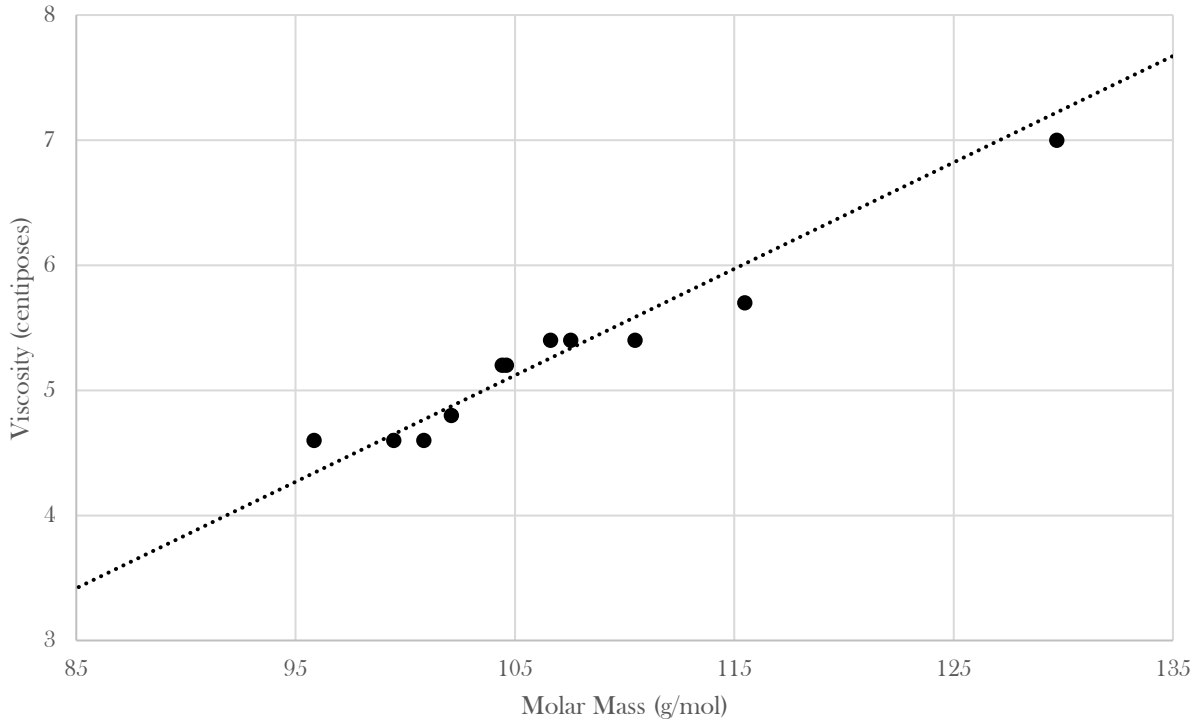


Figure A.1 NaF-$ZrF_4$-$UF_4$ viscosity at 700 °C as a function of the molar mass of each mixture. The dotted line is defined by a slope of 0.0851 centiposes mol $g^{-1}$ and a y-intercept of -3.8159.

As viscosity is expected to follow an exponential temperature dependence, [21] data for 600 and 800 °C was plotted and fit in a similar fashion to Figure A.1. The results for the 50.4-36.4-13.2 mixture were then calculated and extrapolated to derive Eq.9, a formulation for the viscosity's (Pa.s) temperature dependence.

$$\mu = 0.1039e^{-0.0039T(^{\circ}C)} \quad \text{Eq A.2}$$

## A.3. Heat Capacity

Heat capacity has been determined using a Dulong-Petit prediction (Eq A.3), with $N_i$ being the number of atoms per molecule.

$$c_p = \frac{8\Sigma X_i N_i}{\Sigma X_i M_i} \quad \text{Eq A.3}$$

## A.4. Thermal Conductivity

Of the molten salt properties, thermal conductivity is one of the most difficult to measure experimentally. Due to the lack of accurate experimental data, predictive correlations have been difficult to validate. Building on the experience of the solar storage industry, a model based around the rough hard sphere theory [22] has been used as a predictive tool. Eq.7.5 shows the final correlation for thermal conductivity, with R being the ideal gas constant (J $mol^{-1}$ $K^{-1}$), $N_A$ Avogadro's number, $T_M$ the melting point in K, and $C_\lambda$ a translation-rotational coupling constant (Figure A.2) that accounts for the non-spherical shapes of molecules. B is equal to13.28, a constant that has been derived based on fits to accurate more recent experimental data, and F(ξ) is equal to 0.68285 at the salts melting point, and represents a function based on the properties of argon that is expected to be applicable to a wide range of salt compositions.

$$\lambda_i = B \cdot \left(\frac{R^{\frac{3}{2}}}{N_A^{\frac{1}{3}}}\right) \cdot \sqrt{\frac{T_M}{\left(\frac{M_i}{N_i}\right)^{\frac{7}{3}} \cdot \left(\frac{V_i}{M_i}\right)^{\frac{4}{3}}}} \cdot C_\lambda \cdot F(\xi) \quad \text{Eq A.4}$$

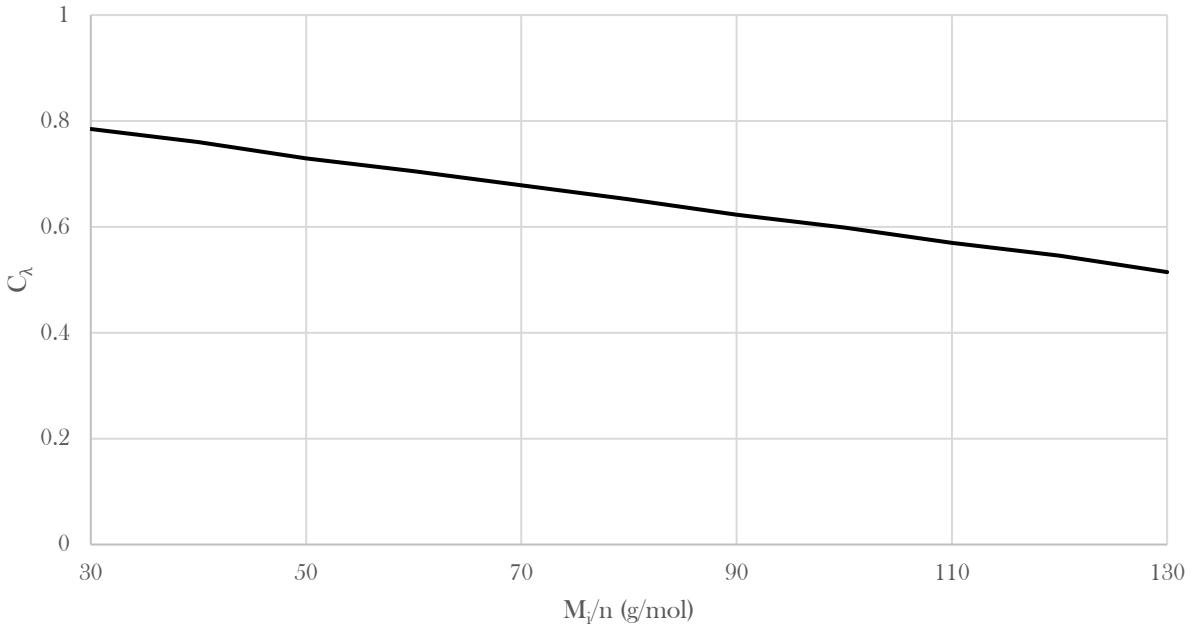


Figure A.2 A fit of Translational-rotational coupling constant ($C_\lambda$) chloride salt experimental data as a function of the ion averaged molecular weight ($M_i$/n). Based on a comparison to limited data for bromide and iodide constituents this line is expected to be a good indication of the trend for all halides salts. [22]

# Appendix B. Thermal Hydraulics

## B.1. Frictional Losses

Frictional losses inhibit the achievement of natural circulation. These losses can be accounted for along flow segments as shown in Eq 4.3. Friction losses are included in the *f* term while additional flow losses due to geometry or area change are included in the K term. Various frictional loss terms have been calculated for the lower plenum, but they are not used as the geometry has not been fully determined and therefore are not shown in this appendix.

### B.1.1. Flow Frictional Loss

$f_i$ is the friction factor for some segment, i, and can be calculated a number of ways, most simply for the case of laminar flow, which is assumed due to low Reynolds numbers that occur:

$$f_i = \frac{64}{Re_i} = 64/\frac{u_i D_i}{\nu} = \frac{64\,\mu}{u_i\,D_i\,\rho} \qquad \text{Eq B.1}$$

### B.1.2. Abrupt Area Change K-loss

Area changes area all assumed to be sharp and abrupt. In reality, these will be sloped or chamfered, but it is conservative to assume they are abrupt.

K-loss for sudden expansion (SE):

$$K_{SE} = K_{cor} \cdot \left(1 - \frac{A_s}{A_L}\right)^2 \qquad \text{Eq B.2}$$

K-loss for sudden contraction (SC):

$$K_{SC} = K_{cor} \cdot \frac{1}{2}\left(1 - \frac{A_s}{A_L}\right)^{\frac{3}{4}} \qquad \text{Eq B.3}$$

### B.1.3. Additional Core K-loss

The K-loss through the core is currently approximated as a PWR core would be, though it will likely be lower because of the flow velocity is much lower, requiring less structural components which contribute to the geometrical k-loss. The formula in Equation B.4 include representative values for upper and lower core plates, and additional frictional losses along the moderator rods typical for fuel assembly rod and spacer grid axial loss.

$$K_{Core} = K_{UpPlate} + K_{LowPlate} + K_{Axial} = 17.20 + 0.093738 \cdot H_{Core} \qquad \text{Eq B.3a}$$

$$K_{Core} = 17.24061 \text{ (Total for 1.5m core)} \qquad \text{Eq B.3b}$$

### B.1.4. Additional Straight Tube Heat Exchanger K-loss

As for the core, additional K-loss for the straight tube heat exchanger is approximated using similar values for PWR SG core bundles straight sections on the secondary side.

$$K_{HX} = 5.747562 \cdot H_{HX} \qquad \text{Eq B.4}$$

### B.1.5. Additional Helical Coil Heat Exchanger K-loss [23]

The helical coil heat exchanger additional k-loss is given for vertical flow through a tube bundle according to Eq B.5:

$$K_{HX} = \phi \cdot A \cdot Re_{HX}^{m} \cdot z + \Delta K_{0,T} \qquad \text{Eq B.5a}$$

where: $A = a_1 b_1 = 1.52\left(\frac{p_R}{d_{o,tube}} - 1\right)^{-0.5}$, $m = -0.2$, $\phi = f(\theta) = 0.54$ , $\Delta K_{0,T} = 0.20552$

$a_1 = 1.52\left(\frac{p_R - d_{o,tube}}{p_H - d_{o,tube}}\right)^{-0.2} = 1.52$ (when axial pitch equals radial pitch)

$b_1 = \left(\frac{p_R}{d_{o,tube}} - 1\right)^{-0.5}$

$\phi$ depends on the inclination angle of the tubes, $\theta = \arctan\left(\frac{p_H}{r_{o,tube}}\right)$, and 0.54 is a conservative estimate.

$z$ = number of transverse rows of tubes in the bundle (The higher of $N_H$ & $N_R$ is chosen for conservativism)

$\Delta K_0 = 2\frac{f(\Delta T)}{T_{cold}} = 0.20552$ (for 600-700°C ΔT)

$$K_{HX} = 0.8208 \cdot Re_{HX}^{-0.2} \cdot z \cdot \left(\frac{p}{d_{o,tube}} - 1\right)^{-0.5} + 0.20552 \qquad \text{Eq B.5b}$$

## B.2. Heat Exchanger Design

The heat transfer area of the heat exchanger affects not only the geometry of the primary loop, but the limits of heat transfer in the system. The general equation for determining overall heat exchanger power (heat removal capacity) is:

$$Q_{HX} = h_{HX}\, A_{HT}\, \Delta T_{HX} \qquad \text{Eq B.6}$$

where: $\Delta T_{HX} = T_{\infty,\text{primary}} - T_{s,HX,primary}$ (difference between bulk fluid avg. and tube surface avg. on primary side)

The temperature difference is set by the desired operational ranges, while the heat transfer area is based on the available area of the heat exchanger annular compartment, depending on if it is a vertical straight tube design or helical coil design. The heat transfer coefficient can be determined from flow conditions in the resulting geometry from the following equation:

$$h_{HX} = \frac{Nu_{mixed} \cdot \kappa}{D_{h,HX}} \qquad \text{Eq B.7}$$

Where the mixed Nusselt number is determined from forced and natural convection terms, which are functions of the Reynolds ($Nu_{Re}$) and Rayleigh ($Nu_{Ra}$) numbers, respectively. The addition/subtraction term is determined by if the natural convection flow is aiding or inhibiting the overall heat transfer.

$$Nu_{mixed} = (Nu_{Re}^{\,3} \pm Nu_{Ra}^{\,3})^{1/3} \qquad \text{Eq B.8}$$

Rayleigh number is a function of the Grasshoff and Prandtl numbers and is calculated from the following function in the heat exchanger:

$$Ra_{HX} = Gr_{HX} Pr = \frac{g\,\beta\,\Delta T_{HX}\, D_{h,HX}^{\,3}\, \rho^2}{\mu^2}\,\frac{c_p \mu}{\kappa} = \frac{g\,\beta\,\Delta T_{HX}\, D_{h,HX}^{\,3}\, \rho^2\, c_p}{\mu\,\kappa} \qquad \text{Eq B.9}$$

Reynold's number is a function of velocity and characteristic dimensions in the channel of interest and is given for the heat exchanger:

$$Re_{HX} = \frac{u_{core}\, \rho\, D_{h,HX}}{\mu}\frac{A_{core}}{A_{HX}} \qquad \text{Eq B.10}$$

B.2.1. Straight Tube Nusselt numbers

The free convection Nusselt number in a vertical channel such as the straight tube heat exchanger is best approximated by the Elenbass correlation [16], which is valid for $10^{-1} \leq \frac{D_h}{H_{HX}} Ra_{HX} \leq 10^5$:

$$Nu_{Ra} = \frac{1}{24} Ra_{HX} \left(\frac{D_h}{H_{HX}}\right) \left(1 - \exp\left[-\frac{35}{Ra_{HX}\left(\frac{D_h}{H_{HX}}\right)}\right]\right)^{3/4} \quad \text{Eq B.11}$$

The forced convection Nusselt number varies for straight tube flow but is well approximated from the Dittus-Boetler correlation [16], which is valid for Re ≥ 10,000:

$$Nu_{Re} = .023 \cdot Re_{HX}^{\frac{4}{5}} \cdot \mathrm{Pr}^{0.3} \quad \text{Eq B.12}$$

Due to the geometry of the heat exchanger, turbulent flow is expected, however, if the flow is fully-developed laminar, the Nusselt number is constant [16] and equal to the following value for constant heat flux:

$$Nu_{Re} = 4.36 \quad \text{Eq B.13}$$

B.2.2. Helical Coil Nusselt Numbers

The free convection Nusselt number for the helical coil is best approximated by flow across horizontal rods, which is valid for $Ra_{HX} \leq 10^{12}$:

$$Nu_{Ra} = \left\{ 0.60 + \frac{0.387\ Ra_{HX}^{1/6}}{\left[1 + \left(\frac{0.559}{Pr}\right)^{\frac{9}{16}}\right]^{8/27}} \right\}^2 \quad \text{Eq B.14}$$

The forced convection Nusselt number with a lower Reynold's number ($50 \leq Re \leq 10{,}000$) for the helical coil is based on the following correlation [24]:

$$Nu_{Re} = 0.6\ Re_{HX}^{0.5}\ \mathrm{Pr}^{0.31} \quad \text{Eq B.15}$$

For high Reynold's numbers ($Re \geq 10{,}000$), the preferred correlation [25] is:

$$Nu_{Re} = 0.36\ Re_{HX}^{0.55}\ \mathrm{Pr}^{1/3}\ \left(\frac{\mu}{\mu_0}\right)^{0.14} \quad \text{Eq B.16}$$

## B.3. Moderator Temperature Profile

B.3.1. Background and Method

The temperature of the hottest rod has been set as a limiting factor in the design, as steady state operation above 800°C is not recommended. [12] The radial heat conduction equation (Eq B.17) has been used to calculate the centerline temperature of the rod, $T_{r_0}$.

$$\frac{1}{r}\frac{d}{dr}\left(kr\frac{dT}{dr}\right) + q''' = 0 \quad \text{Eq B.17}$$

$$Q = q''' \cdot \pi r^2 z = q'' \cdot 2\pi r z = q' \cdot z \qquad \text{Eq B.18}$$

Through integration and using the boundary condition of $q''(r_0) = 0$, Eq B.17 can be used to find the temperature difference across the ZrH portion of the rod (Eq B.19). Using the relationships shown in Eq B.18, the temperature profile can then be written as a function of the volumetric heat rate (Eq B.20).

$$\Delta T_{ZrH} = \frac{q'_{ZrH}}{4\pi k_{ZrH}} \qquad \text{Eq B.19}$$

$$T_{r_0}(z) = T_{r_1}(z) + q'''_{ZrH}(z) \cdot \frac{r_1^2}{4\, k_{ZrH}} \qquad \text{Eq B.20}$$

The volumetric heat rate given above is a function of axial position and is proportional to the flux profile in all regions of the unit cell subchannel and can be represented by the power profile multiplier ($q'''_M$) and flux profile ($\phi(z)$) (Eq B.21).

$$q'''_M = \frac{q''' \cdot L}{\int_0^L \phi(z)\, dz} \qquad \text{Eq B.21}$$

$$q'''(z) = q'''_M \cdot \phi(z) \qquad \text{Eq B.22}$$

The centerline temperature at a given axial position (Eq B.20) can thus be written as (Eq B.23).

$$T_{r_0}(z) = T_{r_1}(z) + q'''_{ZrH_M} \cdot \frac{r_1^2}{4\, k_{ZrH}} \cdot \phi(z) \qquad \text{Eq B.23}$$

Integrating Eq B.17 again and using the condition of flux continuity at the interface of the cladding and moderator, $q''_{ZrH}(r_1) = q''_{SiC}(r_1)$, the temperature difference within the silicon carbide portion of the rod can be obtained (Eq B.24).

$$q''_{SiC}(r_1) = -k_{SiC}\frac{dT}{dr} = q'''_{SiC}\frac{r_1}{2} - \frac{\boldsymbol{C}}{r_1} = q'''_{ZrH}\frac{r_1}{2} \;\rightarrow\; \boldsymbol{C} = (q'''_{SiC} - q'''_{ZrH})\frac{r_1^2}{2} \qquad \text{Eq B.24}$$

$$q''_{SiC} = -k_{SiC}\frac{dT}{dr} = q'''_{SiC}\frac{r}{2} + (q'''_{SiC} - q'''_{ZrH})\frac{r_1^2}{2r} \qquad \text{Eq B.26}$$

$$\Delta T_{SiC} = \frac{q'_{SiC}}{4k_{SiC}\pi} + \frac{r_1^2}{2k_{SiC}}\left(\frac{q'_{SiC}}{\pi(r_2^2 - r_1^2)} - \frac{q'_{ZrH}}{\pi r_1^2}\right)\ln\left(\frac{r_1}{r_2}\right) \qquad \text{Eq B.27}$$

$$T_{r_1}(z) = T_{r_2}(z) + \left[q'''_{SiC_M} \cdot \frac{r_2^2 - r_1^2}{4\, k_{SiC}} - \left(q'''_{SiC_M} - q'''_{ZrH_M}\right) \cdot \frac{r_1^2}{2\, k_{SiC}} \cdot \ln\left(\frac{r_2}{r_1}\right)\right] \cdot \phi(z) \qquad \text{Eq B.28}$$

To calculate the heat generation within each rod, simulations were run in Serpent to obtain both neutron and photon energy deposition (Appendix C). Using the values calculated, in combination with Equations B.19-22, the temperature difference across the radius of the rod can be obtained. However, to calculate the centerline temperature of the rod, this difference must be added to the temperature drop that exists between the rod's surface and bulk fluid. Through the use of flux continuity at the outer surface of the SiC cladding and the heat convection equation, where the heat transfer

coefficient is obtained from mixed (Ra & Re) Nusselt number, the final temperature difference from the surface of the rod to the bulk flowing salt can be calculated (Eq B.30).

$$q''_{salt}(r_2) = q''_{SiC}(r_2) = h\left(T_{r_2} - T_\infty\right) = q'''_{SiC}\frac{r_2}{2} + \left(q'''_{SiC} - q'''_{ZrH}\right)\frac{r_1^2}{2r_2} \quad \text{Eq B.29}$$

$$T_{r_2}(z) = T_\infty(z) + \frac{1}{h}\left(q'''_{SiC_M}\frac{r_2}{2} - \left(q'''_{SiC_M} - q'''_{ZrH_M}\right)\frac{r_1^2}{2r_2}\right)\cdot\phi(z) \quad \text{Eq B.30}$$

The outer boundary temperature is set as the bulk fluid temperature for a given axial height. To obtain the bulk fluid temperature, conservation of energy is applied (Eq B.29).

$$T_\infty(z) = T_\infty(0) + \frac{q'_{res_M}}{\dot{m}\, c_p}\int_0^z \phi(z)\, dz \quad \text{Eq B.31}$$

The resolved linear heat rate (Eq B.32) is calculated from the volumetric heat generation of each subcomponent. The unit cell mass flow rate (Eq B.34) is calculated from conservation of energy across the channel using the change in bulk temperature from inlet to outlet.

$$q'_{res}(z) = q'''_{salt}(z)\cdot(P^2 - \pi\, r_2^2) + q'''_{SiC}(z)\cdot\pi(r_2^2 - r_1^2) + q'''_{ZrH}(z)\cdot\pi\, r_1^2 \quad \text{Eq B.32}$$

$$q'_{res_M}\cdot\phi(z) = \left[q'''_{salt_M}\cdot(P^2 - \pi\, r_2^2) + q'''_{SiC_M}\cdot\pi(r_2^2 - r_1^2) + q'''_{ZrH_M}\cdot\pi\, r_1^2\right]\cdot\phi(z) \quad \text{Eq B.33}$$

$$\dot{m}_{channel} = \frac{Q_{core}}{c_p\,\Delta T_\infty}\cdot\frac{A_{channel}}{A_{core}} \quad \text{Eq B.34}$$

B.3.2. Results

The limit for peak rod temperature ($T_{max}$) was set to 800°C (1073.15K) and the core inlet ($T_{in}$) was set to 600°C (873.15K). As the mass flow rate for the subchannel is set based on the core averages (Eq B.34), the outlet temperature in the hot channel will be higher than the core average at a given flowrate. This ultimately limits the core average ΔT for a given power. This is shown in Figure B.1. For 25MWth, the maximum achievable power, the core average bulk fluid temperature rise is 61.27 K, with a hot channel bulk fluid temperature rise of 157.14 K. The full profile is shown in Figure B.2.

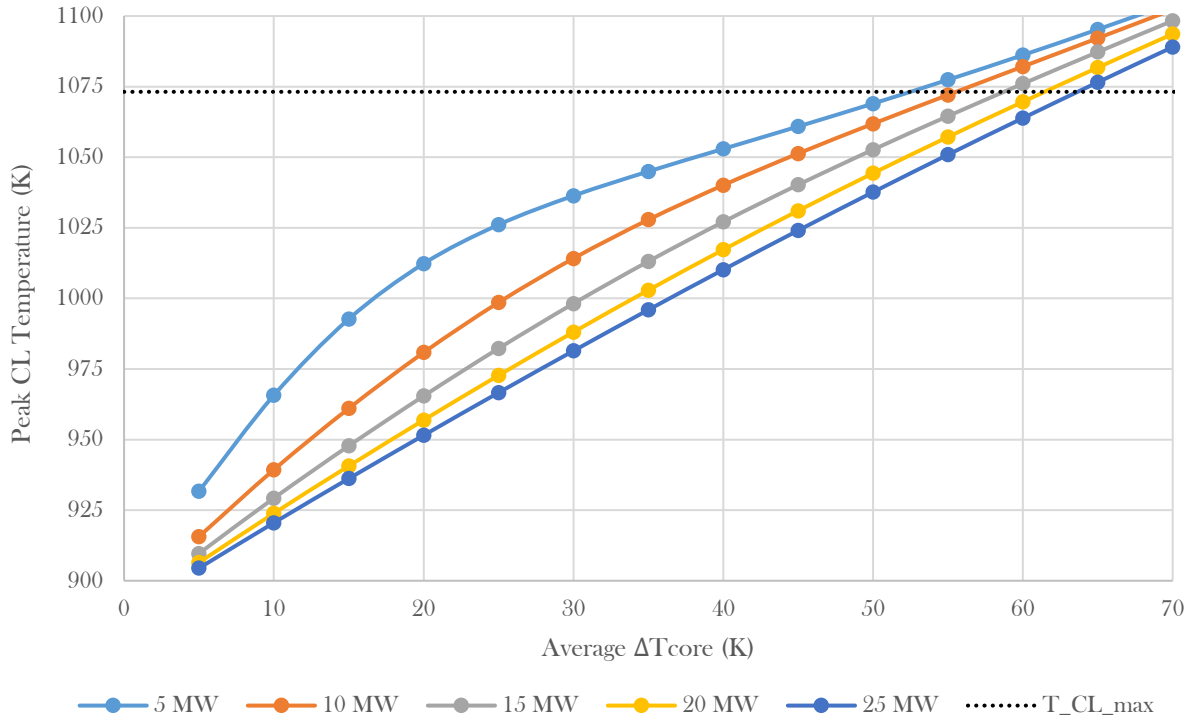


Figure B.1 Peak centerline temperatures for a given reactor power level and average core temperature rise. Notice the limits for core ΔT vary between about 50-60 K, depending on the core power, which correlates to specific design relationships and limits.

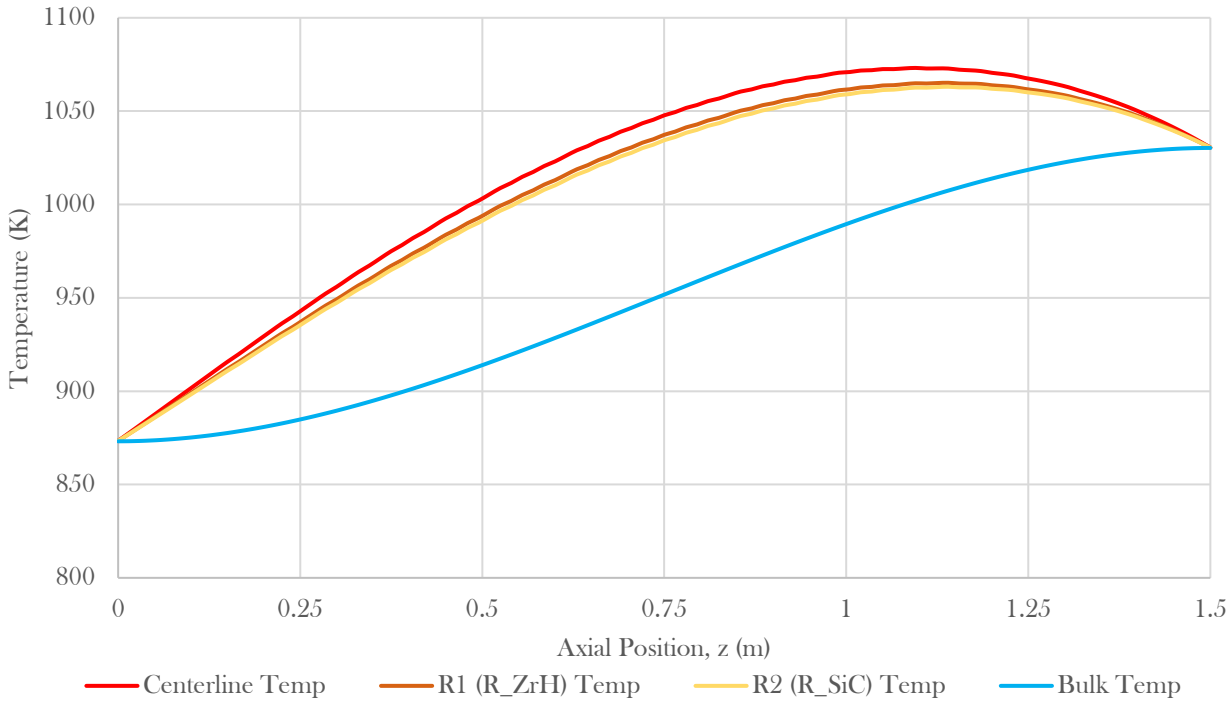


Figure B.2 Temperature profile for bulk fluid, cladding outer, cladding inner/moderator outer, and moderator centerlines in the hottest channel of 25MWth core.

# Appendix C. Reactor Physics

## C.1. Flux Profile

Although the control rod structure displayed in Figure 3.1 is still in need of further optimization, flux profiles for the core geometry have been calculated for both fully inserted and fully removed control rod configurations.

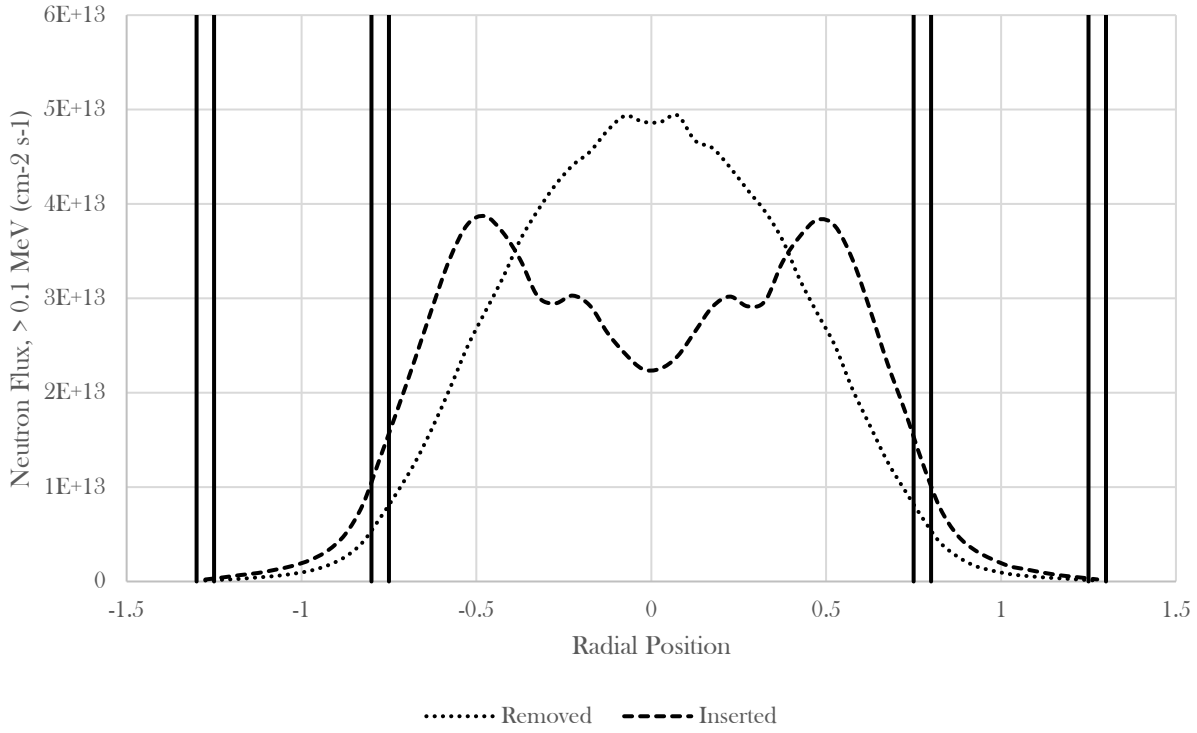


Figure C.1 Neutron flux as a function of radial position for both a fully inserted and fully removed control rod configuration. Flux levels have been normalized to a power level of 25 MWth. Inner and outer vessels are shown with solid vertical lines representing a 0.45 m downcomer thickness.

## C.2. Moderator Heat Deposition

Eq C.1 illustrates the core axial flux profile normalized to an integral of 1, with table C.1 showing the volumetric heat generation present within the central most unit cell.

$$\frac{\phi_z}{\sum_{z=0}^{z=1.5}\phi_z} = -1.7707 \cdot z^2 + 2.6562 \cdot z + 0.0024 \qquad \text{Eq C.1}$$

Table C.1 Volumetric heat generation within the center most unit cell channel. Values have been normalized to be per $MW_{th}$ core power level.

| | Fuel | Moderator | Cladding |
|---|---|---|---|
| $Q'''_{\text{Central Unit Cell}}$ ($W\ m^{-3}\ MW^{-1}$) | 1.26E+06 | 1.10E+05 | 4.63E+04 |

## C.3. Depletion Results

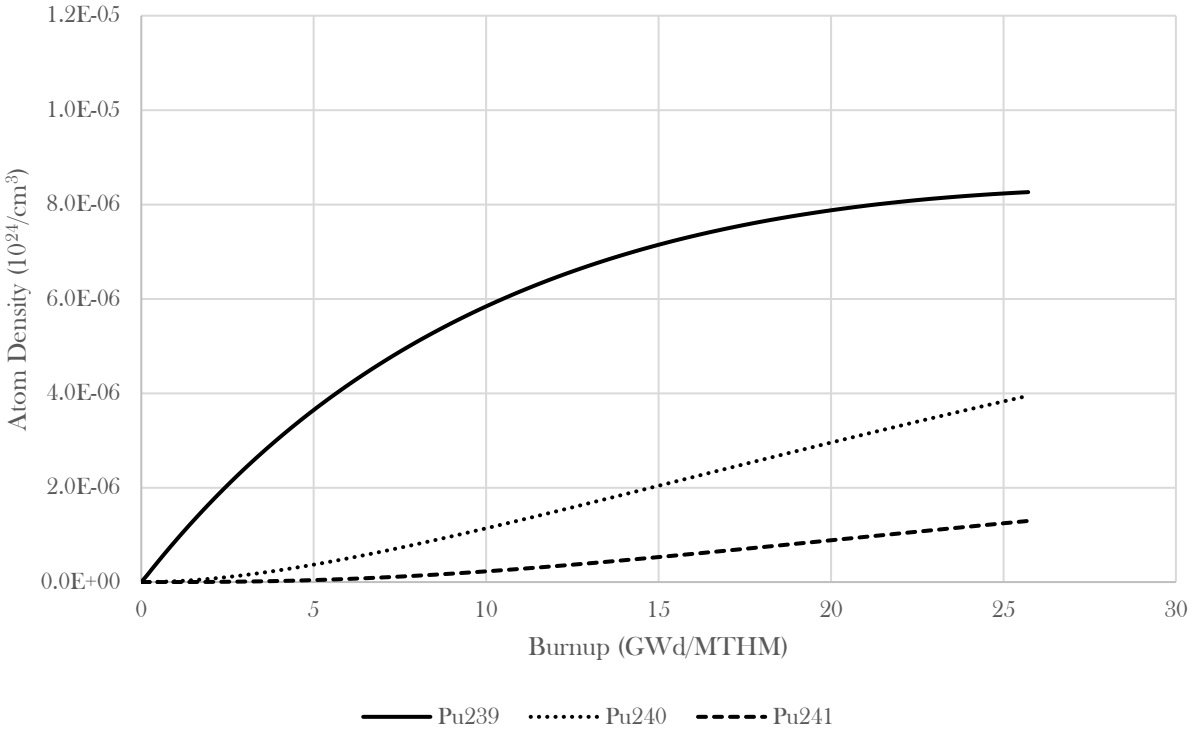


Figure C.2 Primary plutonium isotope concentration as a function of burnup for the TPX reactor.

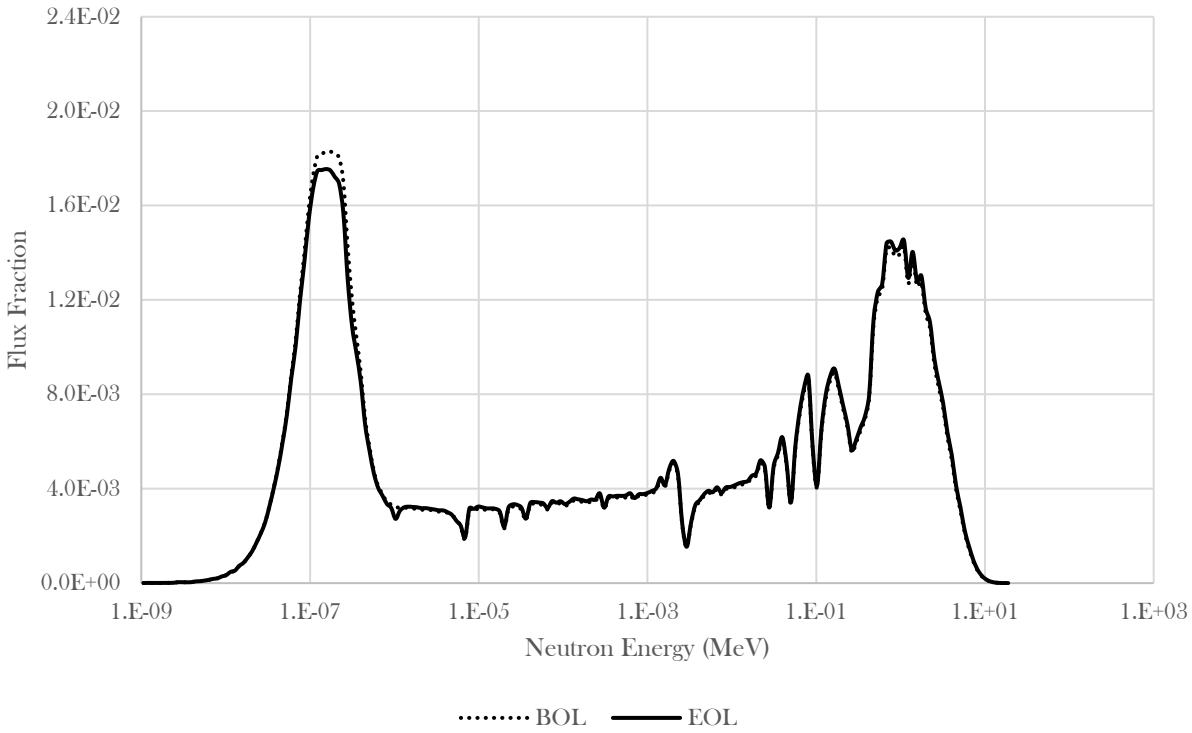


Figure C.3 Neutron spectrum for the beginning of life (BOL), end of life (EOL) TPX fuel composition. EOL is defined by a burnup of 15 GWd MTHM[-1]

# Appendix D. Downcomer Heat Deposition

Table D.1 Power generation (kW) in the downcomer as a function of inner vessel (columns) and downcomer (rows) thickness (m). Values have been normalized to a 50 MW core power level.

| Inner Vessel/Downcomer Thickness (m) | 0.05 | 0.10 | 0.15 | 0.20 | 0.25 | 0.30 | 0.35 | 0.40 | 0.45 |
|---|---|---|---|---|---|---|---|---|---|
| 0.05 | 386 | 262 | 196 | 146 | 108 | 79 | 59 | 43 | 32 |
| 0.10 | 745 | 515 | 388 | 287 | 214 | 157 | 116 | 86 | |
| 0.15 | 1065 | 749 | 560 | 414 | 308 | 227 | 166 | | |
| 0.20 | 1338 | 945 | 703 | 522 | 386 | 285 | | | |
| 0.25 | 1562 | 1107 | 830 | 613 | 452 | | | | |
| 0.30 | 1754 | 1240 | 928 | 688 | | | | | |
| 0.35 | 1903 | 1350 | 1011 | | | | | | |
| 0.40 | 2027 | 1444 | | | | | | | |
| 0.45 | 2814 | | | | | | | | |

## D.1 The Wafer

For molten salt reactors that have a downcomer it is important to limit fission outside of the core, reflect neutrons back into the core, and prevent heat transfer radially from the core. In order to achieve all three of these objectives, a coupled neutron moderator and poison wall is proposed (Figure C.2).

### D.1.1 Design Considerations

The materials contained within the wall or comprising the wall as a whole must have a low thermal conductivity. The core side of the wall must effectively reflect neutrons (low Z, and a low absorption cross-section). The downcomer side of the wall must limit fission in the downcomer region. If materials with high thermal conductivity are to be used, placing the materials in a vacuum or gap material encased in a salt compatible box may serve as a way of limiting thermal conductivity. The vacuum or gap may also serve as an expansion volume if the reflector and poison are prone to swelling when subject to a neutron flux. The wall should not be designed as a safety related system. If the wall were to lose all of its neutron absorption, the reactor should still be able to remain subcritical.

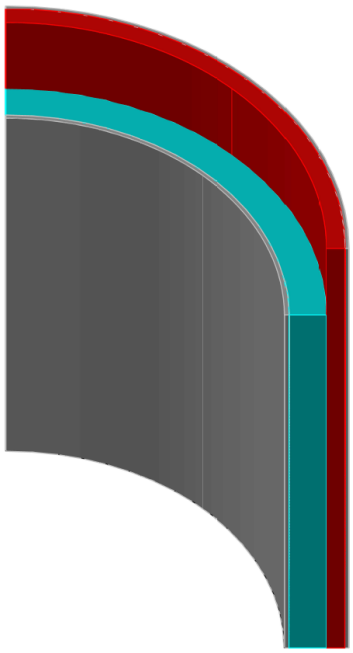

Figure D.1 A conceptual visualization of a layered inner vessel wall for molten salt reactors containing a downcomer. In this figure red indicates a neutron poison such as $Gd_2O_3$-$Al_2O_3$, teal indicates a neutron moderator such as graphite, and grey indicates a salt compatible lining if required.

D.2.2 Results

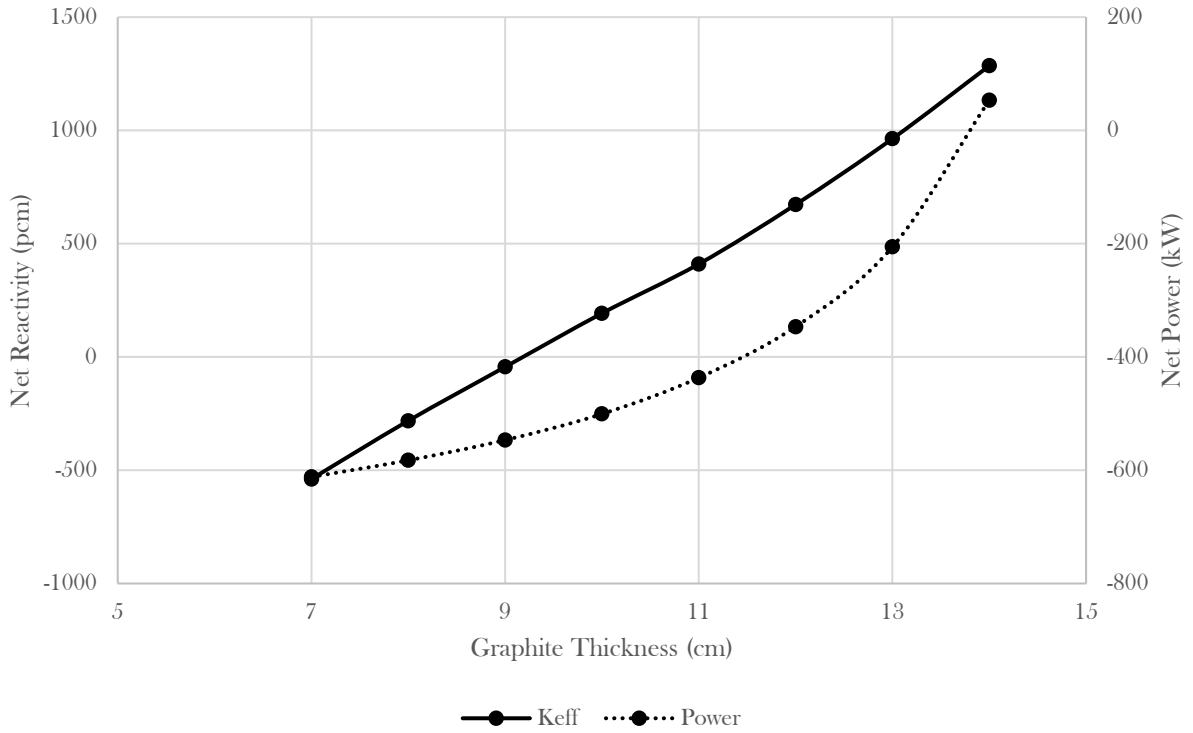


Figure D.2 Net reactivity and power generation in the downcomer as a function of graphite thickness in a 15 cm inner vessel. Please note that net is in reference to a 15 cm 800 H inner vessel, with a downcomer thickness of 35 cm.

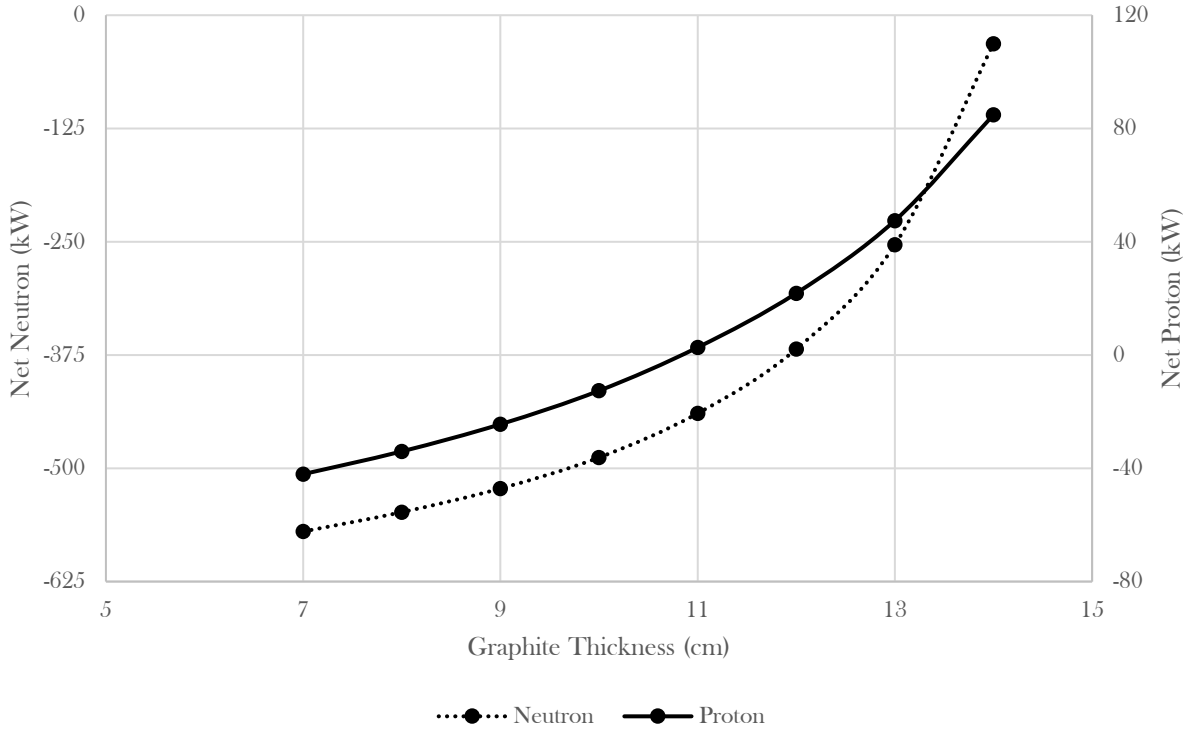


Figure D.3 Net neutron and proton power generation in the downcomer as a function of graphite thickness in a 15 cm inner vessel. Net is in reference to a 15 cm 800 H inner vessel, with a downcomer thickness of 35 cm.

# Appendix E. Cost Analysis

## E.1 Zirconium Hydride

Data from a German compact sodium cooled reactor project [12] indicated that delta phase zirconium hydride rods could be manufactured for 45 to 65 US$ $kg^{-1}$ in 1964. This value gives no indication of cost as a function of scale, however, accounting for inflation, an estimate of 350 to 500 US$ $kg^{-1}$ is obtained. TPX as currently designed contains 1488 moderator rods (3.2 tons of ZrH) leading to an upper cost estimate of 1.6 million US$.

## E.2 Silicon Carbide

The cost of the moderator rod cladding varies widely depending on the form of silicon carbide used. However, as CVD SiC appears to provide the best performance for the TPX application (specifically, high thermal conductivity after irradiation) cost estimates for the fabrication of 1,500 tubes were obtained for the CVD process. Based on conversations with leading ceramic manufacturers a unit cost of 8,383 US$ $tube^{-1}$ can be expected.

## E.3 Fuel Salt

Eliminating lithium from the TPX fuel salt makes the overall salt cost highly dependent on the actinide composition and relative quantity. The TPX fuel salt carries a uranium mass fraction of 0.2543 with the cost for 5% enriched uranium sitting at around 1,400 US$ $kg^{-1}$ as of August 14th 2017. [33] the weight fraction of NaF and $ZrF_4$ is 0.1714 and 0.4930 respectively with the cost of the constituents expected to be on the order of 1.32 and 16.8 US$ $kg^{-1}$. [8]

## E.4 Integral Vessel

Using a Incoloy 800H/Ni201 composite instead of Hastelloy N looks to offer significant cost savings for large scale structural components. 800H currently costs around 8 US$ $lb^{-1}$ while Hastelloy N is upwards of 100 US$ $lb^{-1}$. The Ni201 overlay adds approximately 3,041 US$ $m^{-2}$. [34]

## E.6 Heat Exchanger

As no manufacturing input has been obtained for the heat exchange cost at this time, the current estimate uses solely the material cost of Ni201.

## E.7 Balance of Plant

Using a gas turbine, initial estimates for power generation components (turbine, generator, compressor etc.) show a decrease in levelized cost as we move to higher power levels (Eq. E.1). The formulation has been created using data from [35] and a constant 40 % electrical efficiency.

$$Cost(\$) = 0.4393 \cdot Power(W_{th}) + 7.3309 \cdot 10^6 \qquad \text{Eq. E.1}$$

# Appendix F. Stress Analysis

## F.1. Background

Flow Induced Vibration (FIV) causes damage via two mechanisms: fatigue (dynamic stresses) and fretting (surfaces wearing due to mutual contact from cyclical motion). FIV effects are expected to be determined through coupling of stress analysis code DIABLO, and computation fluid dynamic code Nek5000.

Additional stresses induced by the weight of the fluid and kinetic energy of the flow are also of interest throughout the vessel and on major components such as the heat exchanger and moderator rods.

## F.2. Vessel Stress

The vessel is not expected to be affected significantly by flow induced vibration, however, the larger volume of dense fuel salt does place design limits on the vessel thickness, and may affect the standards to which the vessel would need to qualify.

The maximum (hydro)static pressure occurs at the bottom of the vessel, within the lower plenum. Thus, we will primarily be concerned with hoop stresses on the outer vessel and pressure along the (weld) seams where the base and outer vessel meet. The principal stresses at the inside wall are tangential (hoop) stress, $\sigma_t$, radial stress, $\sigma_r$, and axial stress, $\sigma_a$. These principle stresses are expressed below.

$$\sigma_t = P_i \frac{r_o^2 + r_i^2}{r_o^2 - r_i^2} \quad \text{Eq F.1}$$

$$\sigma_r = -P_i \quad \text{Eq F.2}$$

$$\sigma_a = P_i \frac{r_i^2}{r_o^2 - r_i^2} \quad \text{Eq F.3}$$

In (Eqs F.1-3), $P_i$ is the internal pressure, which will be the stagnation pressure (Eq F.4) at steady state flow. The static pressure is substituted for the stagnation pressure in the results presented in Table 2 as the kinetic energy contribution is orders of magnitude lower than the static contribution.

$$P_{stagnation} = P_{static} + \frac{1}{2}\rho v^2 \quad \text{Eq F.4}$$

For solution heat treated Incoloy 800H, the minimum yield strength is approximately 100 MPa, so stresses induced by the flow against the vessel are not expected to be of concern. Setting the minimum yield as the value of tangential stress, the minimum thickness can be calculated from (Eq F.1), as shown in the last column of Table F.1.

Table F.1 Vessel geometry, static pressure, principle stresses (assuming thickness of 5cm), and resulting minimum vessel thickness.

| Parameter | Value |
|---|---|
| Vessel Internal Height (m) | 3.1 |
| Vessel Internal Diameter (m) | 1.7 |
| Static Pressure (kPa) | 113.18 |
| Tangential Stress (MPa) | 1.98 |
| Radial Stress (MPa) | -0.11 |
| Axial Stress (MPa) | 0.93 |
| Minimum Vessel Thickness (cm) | 0.09363 |

## F.3. Moderator Rods

Moderator rods are expected to be subject to some of the most intensive FIV as the fluid is heating and accelerating in the core region. These FIV must be evaluated to determine if additional structural supports are necessary. Additionally, the moderator rods experience an external stagnation pressure from the flowing fuel and an internal pressure either from designed backpressure or possible off-gassing of hydrogen. Each stress must be evaluated individually to determine which is the limiting design stress for cladding thickness.

The maximum external static stresses from the fluid can be assumed to equal the same maximum internal static pressure the vessel experiences. The internal stresses have not been determined. Additionally, the manufacturing method of the SiC cladding has significant impact on the final strength, but CVD is assumed here. For CVD SiC, the lowest experimentally reported flexural strength is 353 MPa, internal pressurization strength (tangential yield) is 301 MPa, and compressive strength of ~200 MPa (NOTE: the compressive strength is based on creep occurring when a compressive load was applied at an angle. There is not available data for radial compression). [36] Assuming these stress limits, a maximum allowable pressure can be determined from (Eq F.1).

Table F.2 Approximate maximum allowable pressures for moderator rod cladding with thicknesses (t) from .1-1 mm and stress of 200 MPa.

| ZrH Diameter (mm) | Max Pressure (MPa) t = .1 mm | Max Pressure (MPa) t = .5 mm | Max Pressure (MPa) t = 1 mm |
|---|---|---|---|
| 0.018 | 1.108 | 5.478 | 10.803 |

## F.4. Heat Exchanger

The heat exchanger is the other component of major concern with regards to FIV due to the intricate geometry and heat transfer within the exchanger region. The external pressures from the flowing fuel are expected to be negligible compared to the design limits on internal pressure set by the pressure of the tertiary loop in the case of breaks from tertiary to secondary.

Piping design code falls under ASME B 31, including B31.1 (Power Piping) and B 31.3 (Process Piping), in addition to many others. ASME B 31.3 gives requirements for minimum pipe thickness based on pipe outer diameter ($D_o$), design pressure (P), allowable stresses (S), and weld specifications (E & W), and code case factors ($\gamma$), summarized in (Eq F.5). An alternative method [37] of calculating minimum thickness based on allowable displacement (d) is also shown in (Eq F.6). Note: E in (Eq F.6) represents the modulus of elasticity, not a weld quality factor.

$$t = \frac{P \cdot D_o}{2(S \cdot E \cdot W + P \cdot \gamma)} \qquad \text{Eq F.5}$$

$$t = \frac{P \cdot D_i^2}{4 \cdot d \cdot E} \rightarrow \quad t = \frac{\sqrt{E}\sqrt{d}\sqrt{2DP + Ed} + DP + Ed}{2P} \qquad \text{Eq F.6}$$

With the assumption that tertiary pressure is 1.876 MPa (based on the CTAHs [38]) all weld and code factors are 1 (nominal) or 0.5 (conservative), and the allowable stress assumed to be ~80 MPa (based on temperature transients up to ~1100K), required pipe thickness for the varying outer diameters (as allowed by the natural circulation script) can be calculated and are shown in Table F.3.

Table F.3 Estimated pipe thickness requirements ($t_{req}$) and resulting pipe inner diameters ($D_i$) based on pipe outer diameter ($D_o$) and code factors.

| | $D_o$ (mm) | 10 | 20 | 30 | 40 | 50 |
|---|---|---|---|---|---|---|
| Nominal Code Factor | $t_{req}$ (mm) | 0.11 | 0.23 | 0.34 | 0.46 | 0.57 |
| Values: (E=W=γ=1) | $D_i$ (mm) | 9.77 | 19.54 | 29.31 | 39.08 | 48.85 |
| Conservative Code Factor | $t_{req}$ (mm) | 0.45 | 0.90 | 1.34 | 1.79 | 2.24 |
| Values: (E=W=γ=0.5) | $D_i$ (mm) | 9.10 | 18.21 | 27.31 | 36.42 | 45.52 |
| Displacement method: | $t_{req}$ (mm) | 0.49 | 0.50 | 0.51 | 0.52 | 0.53 |
| (d = 1 mm) | $D_i$ (mm) | 9.02 | 19.00 | 28.98 | 38.96 | 48.94 |